

**Department of Physics and Astronomy  
Heidelberg University**

Master thesis in Physics  
submitted by

**Rohan Kulkarni**  
born in Thane, India

handed in on  
**September 30, 2022**



# **Axion Basinschein : A search for gravitationally bound solar axions via stimulated decay into photons**

This master thesis has been carried out by Rohan Kulkarni at the  
**Faculty of Physics at McGill University and**  
**Institute of Theoretical Physics at Heidelberg University** under the  
supervision of  
**Prof. Dr. Katelin Schutz and Prof. Dr. Joerg Jaeckel**



## Acknowledgements

First of all, I have to thank Prof. Katelin Schutz for giving me the opportunity of working under their guidance for this thesis. She has been highly supportive throughout the entire course of this thesis, both academically and otherwise. Apart from physics, I learned the tools required to perform research efficiently under her supervision. Further, I thank Prof. Joerg Jaeckel for agreeing to be the co-supervisor for this thesis and for giving constructive feedback throughout the thesis.

I am glad for the fruitful collaboration with Yitian Sun and would like to thank him for being an excellent collaborator. Apart from that, I would also like to thank all my colleagues from DMcGill. Particularly Nirmalya Brahma and Saniya Heeba for being excellent colleagues, and also being there in times of need as friends.

Last but not least, I express my deep gratitude to my family and friends for their tremendous support. In particular, I thank my wife for constantly pushing me to aim for the stars.



## Abstract

A recent study has found that massive particles like axions emitted from stars can enter gravitationally bound orbits around them. These particles then accumulate over the large astronomical lifetime of the star, forming a density profile around them called stellar basins. This density profile is known as the solar axion basin. In another study, it has been established that an electromagnetic signal with a wavelength corresponding to half of the axion mass produces a stimulated decay of axions into photons, which we call an echo. The geometry of this echo is such that the axion decays into two back-to-back facing photons. This master's thesis combines these ideas to predict echo signals from axion stellar basins of various stellar objects, which we call basinschein. First, we predict the echo of keV axions from the basin of our sun, a white dwarf, and a neutron star. Secondly, consider the axion basin of our sun for various axion masses and predict their echo signals. Then, we estimate an echo signal from Milky Way's dark matter halo. The echo signal from all these scenarios is too weak to be detected by past and present instruments; hence, it is improbable that we find a signature of such a phenomenon in current and archived data.

## Zusammenfassung

Eine kürzlich durchgeführte Studie hat herausgefunden, dass massive Teilchen wie Axionen, die von Sternen emittiert werden, in gravitativ gebundene Umlaufbahnen um sie herum eintreten können. Diese Partikel sammeln sich dann über die große astronomische Lebensdauer des Sterns an und bilden um sie herum ein Dichteprofil, das als stellare Becken bezeichnet wird. Dieses Dichteprofil ist als solares Axionbecken bekannt. In einer anderen Studie wurde festgestellt, dass ein elektromagnetisches Signal mit einer Wellenlänge, die der Hälfte der Axionmasse entspricht, einen stimulierten Zerfall von Axionen in Photonen hervorruft, den wir als Echo bezeichnen. Die Geometrie dieses Echos ist derart, dass das Axion in zwei Rücken an Rücken gegenüberliegende Photonen zerfällt. Diese Masterarbeit kombiniert diese Ideen, um Echosignale von Axion-Stellarbecken verschiedener Sternobjekte vorherzusagen, die wir Beckenschein nennen. Zuerst sagen wir das Echo von keV-Axionen aus dem Becken unserer Sonne, eines Weißen Zwergs und eines Neutronensterns voraus. Betrachten Sie zweitens das Axionbecken unserer Sonne für verschiedene Axionmassen und sagen Sie deren Echosignale voraus. Dann schätzen wir ein Echosignal aus dem Halo aus dunkler Materie der Milchstraße. Das Echosignal all dieser Szenarien ist zu schwach, um von früheren und gegenwärtigen Instrumenten erkannt zu werden; Daher ist es unwahrscheinlich, dass wir in aktuellen und archivierten Daten eine Signatur eines solchen Phänomens finden.



# Contents

<b>1</b>	<b>Introduction</b>	<b>16</b>
<b>2</b>	<b>Axions</b>	<b>18</b>
2.1	Strong CP problem . . . . .	18
2.2	QCD Axion . . . . .	21
2.3	Axion Like Particles (ALPs) . . . . .	23
2.4	Axion Production: Misalignment Mechanism . . . . .	24
2.5	ALP Dark matter . . . . .	26
2.6	Axion Searches . . . . .	26
2.6.1	Detection principle . . . . .	26
2.6.2	Haloscopes . . . . .	27
2.6.3	Light Shining Through Walls (LSW) experiments . . . . .	29
2.6.4	Helioscopes . . . . .	30
<b>3</b>	<b>Production of axion echo</b>	<b>32</b>
3.1	Axion echo from a point source . . . . .	32
3.2	Stimulated emission of axions in a photon bath . . . . .	33
<b>4</b>	<b>Stellar Basins</b>	<b>34</b>
4.1	Idea : Basin Formation . . . . .	35
4.2	Calculation : Basin Formation . . . . .	35
4.3	Solar Axion Basin . . . . .	39
4.3.1	Process 1 : Axion-Bremsstrahlung . . . . .	39
4.3.2	Process 2 : Axion-Compton scattering . . . . .	41
<b>5</b>	<b>Axion Basinschein</b>	<b>43</b>
5.1	keV Axion Basinschein . . . . .	44
5.1.1	keV solar axion basin . . . . .	44
5.1.1.1	Case I : Quiet Sun . . . . .	45
5.1.1.2	Case II : Solar Flares . . . . .	46
5.1.2	Axion forwardschein from a white dwarf basin . . . . .	47
5.1.3	Axion forwardschein from a neutron star axion basin . . . . .	48
5.1.4	Projected photon numbers . . . . .	49

5.2	Solar Axion Basinschein . . . . .	50
5.2.1	Solar basinschein : Ultraviolet (UV) . . . . .	51
5.2.2	Solar basinschein : Optical (OP) . . . . .	52
5.2.3	Solar basinschein : Infrared (IR) . . . . .	52
5.3	O-star forwardschein estimate . . . . .	53
<b>6</b>	<b>Axion Haloschein</b>	<b>56</b>
6.1	Axion Haloschein from the solar optical band . . . . .	58
6.2	Axion forwardschein from a distant radio galaxy source . . . . .	61
6.2.1	Cosmological integrated DM density . . . . .	62
6.2.2	Dwarf Galaxy . . . . .	64
6.3	Projected SNR . . . . .	65
<b>7</b>	<b>Conclusion</b>	<b>67</b>
<b>References</b>		<b>69</b>
<b>A</b>	<b>FLRW axion misalignment</b>	<b>76</b>
<b>B</b>	<b>Axion Electrodynamics</b>	<b>79</b>
B.1	Axion Klein-Gordon equation . . . . .	79
B.2	Axion Maxwell equation . . . . .	81
<b>C</b>	<b>Axion Echo</b>	<b>84</b>
<b>D</b>	<b>Energy loss rate for axion production via axion-bremstrahlung</b>	<b>88</b>
<b>E</b>	<b>Dark Currents for CCD</b>	<b>91</b>

# List of Figures

2.1	CPT transformations of a neutron. The figure is taken and modified from [16]. . . . .	20
2.2	<i>Left:</i> A classical picture of the neutron ; <i>Right:</i> Axion solution to the Strong CP problem, a dynamical angle between the up and down quarks will be set such that the neutron relaxes itself to the minimum energy configuration without a dipole moment. This dynamic angle is called the axion. The figure is taken from [17]. . . . .	20
2.3	The Vacuum Realignment Mechanism. At temperatures $T = f_a$ , the complex Peccei-Quinn scalar field develops its vacuum expectation value and breaks the global $U(1)_{PQ}$ symmetry. The figure and its description is taken from [19]. . . . .	22
2.4	Evolution of axion ( $\phi \rightarrow \theta$ in our calculation) quantities in the exact solution to the background evolution of an ALP for a radiation-dominated universe. The figure and its description is taken from [20]. . . . .	25
2.5	Schematic of a Haloscope. The figure is taken from [28]. . . . .	27
2.6	Axion-Photon coupling parameter space, zoomed in on Haloscope bounds. The figure is taken from [31]. . . . .	28
2.7	Schematic of a dielectric haloscope. The figure is taken from [33]. . . . .	28
2.8	Schematic of an LSW experiment. The figure is taken from [28]. . . . .	29
2.9	Excluded parameter space for axion-photon coupling from Haloscopes, Helioscopes, and LSW experiments. The figure is taken from [28]. . . . .	30
2.10	Schematic of a Helioscope experiment. The figure is taken from [28]. . . . .	31
4.1	Black curve: A generic differential energy loss rate per unit volume $dQ/d\omega$ per energy $\omega$ of the emitted particle. The blue sliver represents the nonrelativistic modes gravitationally bound to the star. The figure and its description is taken from [9]. . . . .	36
4.2	Feynman diagram for Axion-Bremsstrahlung. . . . .	39
4.3	Feynman diagram for axion-Compton scattering process. . . . .	41

4.4 Axion energy density at Earth's surface from the solar basin denoted $\rho_b$ , plotted as a function of axion mass $m$ , and $g_{aee} = 3 \times 10^{-13}$ . The relativistic solar flux is denoted by $\rho_\infty$ . The axion energy density is plotted for conservative, fiducial and optimistic basin lifetimes corresponding to $10^7, 10^8$ and $4.5 \times 10^9$ years, respectively. Golden curves correspond to contribution to the basin density from axion-bremsstrahlung, and the red curves correspond to contribution from axion-Compton scattering. The figure and its description is taken from [9]. . . . .	42
5.1 An extreme solar flare X-ray event in frequency $\nu \in [0.1, 0.8]$ nm recorded on 6 Sept 2005. The figure is taken from [46]. . . . .	47
5.2 Spectrum of solar radiation. The figure is taken from [52]. . . . .	50
5.3 <i>Top:</i> Flux density of sun versus an O-star ( $T = 50000$ K) in the wavelength $\lambda \in [0, 500]$ nm. <i>Bottom:</i> Flux density of sun versus an O-star in the wavelength $\lambda \in [0, 1500]$ nm . . . . .	54
6.1 Milky Way's DM halo density modeled using the NFW profile . . . . .	56
6.2 Schematic for gegenschein geometry from the Milky Way's DM halo. The figure is inspired from [34] . . . . .	57
6.3 Gaussian wavepacket created in Mathematica to compute the SNR from Hubble's STIS exposure time calculator . . . . .	60
6.4 Spectral flux density of Cygnus A as a function of frequency . . . . .	61
6.5 <i>Left:</i> Integrated dark matter column density from redshift $z \in [0, 1]$ in an expanding $\Lambda$ CDM universe ; <i>Right:</i> Integrated dark matter column density from redshift $z \in [0, 5]$ in an expanding $\Lambda$ CDM universe . . . . .	63
6.6 Dark matter density profile of dwarf galaxy Leo I plotted as a function of distance from the center of the halo . . . . .	64
E.1 <i>Left:</i> Band structure of electron energy in a solid. <i>Right:</i> The difference between the band gaps in insulators, metals, and semiconductors. The figure is taken from [61]. . . . .	91

# List of Tables

5.1	Summary of all basinschein and haloschein scenarios estimated in chapter 5 and 6. . . . .	44
5.2	Summary of keV basinschein photons estimated by Chandra X-ray observatory from axion basins of the sun, a white dwarf and a neutron star. . . . .	49





# Chapter 1

## Introduction

Astroparticle physics is a relatively new and rapidly expanding field of study that examines the behavior and effects of particles emitted from stellar objects. Although astroparticle physics has been around for only a few decades, its potential applications are vast and continue to grow exponentially. In addition to studying the particles themselves, astroparticle physics also investigates the effects that these particles have on other objects in space. Astroparticle physics can also help us to understand the nature of dark matter. By better understanding the particles that make up our universe, we can gain a greater understanding of the universe as a whole.

Axions are hypothetical particles predicted by various extensions to the Standard Model of particle physics. They were originally proposed to solve the strong CP problem in quantum chromodynamics [1]. These particles are very weakly interacting [2–4], and so far have evaded detection. However, they may be produced in the early universe [5] and could make up a significant fraction of the dark matter in the universe [6], as well as play a role in matter-antimatter asymmetry [7].

There are various ways to search for axions, including haloscopes, helioscopes, and laser interferometer experiments. Most of these experiments use a magnetic field to convert axions into photons, which can then be detected. There are several astrophysical and cosmological constraints on the properties of axions. One strong astrophysical constraint comes from the Helium burning lifetime of globular cluster stars, which constrains the axion-photon coupling to be less than  $10^{-10} \text{ GeV}^{-1}$  [8]. Other constraints come from the effects of axions on the cosmic microwave background, the large-scale structure of the universe, and the abundance of axions in the early universe. A detailed summary of astrophysical axion constraints can be found in [8].

Most axions produced in stellar objects like the sun escape into deep space. Still, a tiny fraction of particles enters gravitationally bound orbits around the sun due to their non-null mass. These bound axions form a density profile

around the stellar object by accumulating over the astronomical lifetimes of these objects. This density profile is called as axion basin [9].

According to quantum field theory, pseudoscalars like axions that interact with the electromagnetic force can decay into two photons via the chiral anomaly [10]. But, they have lifetimes larger than the age of our universe. When these axion basins are irradiated by photons having a frequency half their mass, they boost the decay rate of the axions, which in turn significantly reduces their lifetimes [11, 12]. The geometry of such a process, where the decay rate is boosted, produces two back-to-back photons. We call this stimulated decay of axions into photons as axion echo (In contrast to the literature, where axion echo is referred to as a signal corresponding to only one of the two photons).

This thesis's subject is to astrophysically constrain the axion-photon coupling  $g_{a\gamma\gamma}$  by indirect detection of axions that are gravitationally bound to various stellar objects. To constrain the axion-photon coupling, we estimate the probability of detecting photons emitted due to the stimulated decay of photons from different stellar basins. We call this phenomenon axion basinschein. Furthermore, we look for photons emitted by stimulated decay from the Milky Way's (MW) Dark Matter (DM) halo. We call this axion haloschein.

To clarify other nomenclatures, if we observe the axion echo in the direction of the source stimulating the decay, we call it forwardschein (as we will be observing forward decayed photons from the perspective of the source). Suppose we are looking for the axion echo in the direction opposite to the stimulating source. In that case, we call it gegenschein (as we will observe the back decayed photon from the source's perspective). In literature, the terms "axion echo" and "axion gegenschein" are used interchangeably depending on the author's preference. In this thesis, we will estimate axion echos by assuming that the photon sources that stimulate our decay are point sources. On the other hand, the gegenschein geometry can get quite intricate, especially if we are not observing a point source. An excellent description of a generic gegenschein geometry is discussed in [13]. Estimates for various echo/gegenschein signals in literature have been performed and can be found in [11, 13, 14].

# Chapter 2

## Axions

### 2.1 Strong CP problem

Historically speaking, the strong CP problem theoretically motivated the existence of an axion. Following [10] and [15], we will start with a brief yet self-contained summary of the strong CP problem. Let us start by looking at the gluon self-dynamics terms in the SU(3),

$$\mathcal{L}_{\text{QCD}} \supset -\frac{1}{4}G_{\mu\nu}^a G^{\mu\nu a} + \frac{g^2}{32\pi^2}\theta\tilde{G}_{\mu\nu}^a G^{\mu\nu a}, \quad (2.1)$$

where  $\tilde{G}_{\mu\nu}^a = \frac{1}{2}\epsilon_{\mu\nu\sigma\tau}G^{\sigma\tau a}$ .

$G_{\mu\nu}^a$  is the gluon field strength tensor. The first term here comes from the typical kinetic term of the gluon field. It is *CPT* invariant i.e. individually invariant under  $C$ ,  $P$ , and  $T$ . The second term comes into the equation when you contract the  $G_{\alpha\beta}^a G_{\gamma\delta}^a$  with  $\epsilon^{\alpha\beta\gamma\delta}$ . This term breaks *CP* symmetry (*CPT* is still conserved). This is a problem as experimentally; we do not observe *CP* violation in strong interactions.

One way to satisfy this would be to take the  $\theta = 0$  by assuming the  $G\tilde{G}$  term to be a boundary term, i.e., a total derivative of a 4-current, and then we can safely ignore it. This is done by taking a Chern-Simons current,

$$K_\mu = \frac{1}{2}\epsilon_{\mu\alpha\beta\gamma} \left[ A_\alpha^a G_{\beta\gamma}^a - \frac{g}{3}f^{abc}A_\alpha^a A_\beta^b A_\gamma^c \right], \quad (2.2)$$

which can be written as,  $\epsilon^{\mu\nu\alpha\beta}F_{\mu\nu}^a F_{\alpha\beta}^a = \partial^\mu K_\mu$ . (2.3)

An important thing to note here would be that total derivatives never contribute to perturbation theory. This is because the Feynman rule of such a term would have a factor of the sum of all momenta going into the vertex minus the momenta going out - which gives a zero. This means that such a term could only contribute to non-perturbative effects.

We can see another interesting aspect of this problem by introducing the first generation of quarks interacting with the gluons. In this toy model, we assume these quarks have inherited mass from the Higgs via a Yukawa-type coupling after spontaneous symmetry breaking, giving us the following Lagrangian,

$$\mathcal{L} = -\frac{1}{4}G_{\mu\nu}^a G^{\mu\nu a} + \frac{g^2}{32\pi^2}\theta\tilde{G}_{\mu\nu}^a G^{\mu\nu a} + \bar{q}_L iD^\mu q_L + \bar{q}_R iD^\mu q_R - (m\bar{q}_L q_R + m^* \bar{q}_R q_L). \quad (2.4)$$

For the  $m$  to be mass, we need it to be real. If we assume  $m = |m| e^{i\alpha}$ , then we can use a axial  $U(1)_A$  rotation,

$$q_L \rightarrow q_L e^{i\frac{\alpha}{2}}, \quad (2.5)$$

$$q_R \rightarrow q_R e^{-i\frac{\alpha}{2}}, \quad (2.6)$$

to eliminate the phase and make  $m$  real. The left and right-handed fields are rotated in the opposite direction under this symmetry. This  $U(1)_A$  symmetry induces CP violation in strong interactions via loop diagrams. This is called the axial or chiral anomaly. After performing this rotation (and a lengthy calculation associated with it which we skipped), we get an additional term in the Lagrangian,

$$\mathcal{L} \rightarrow \mathcal{L} + \frac{g^2}{32\pi^2}\alpha G_{\mu\nu}^a G^{\mu\nu a}. \quad (2.7)$$

This term is strikingly similar to the CP violating term in eq. (2.1). We can now define a new variable,  $\bar{\theta} \equiv \theta + \alpha$ ,

such that we get a term like,

$$\mathcal{L}_{\text{QCD}} \supset \frac{g^2}{32\pi^2}\bar{\theta}\tilde{G}_{\mu\nu}^a G^{\mu\nu a}, \quad (2.9)$$

in our Lagrangian. Hence, if we get  $\bar{\theta} = 0$ , our Lagrangian will be CP-symmetric again. But, if we perform another axial rotation, our quark mass will be complex again. The only way  $\theta \rightarrow 0$  is when the  $\theta$  and  $\alpha$  terms cancel each other perfectly in  $\bar{\theta}$ . This seems to be by pure chance, and the strong CP problem questions the reasoning behind the exact cancellation of these terms.

We know that electroweak theory violates CP symmetry. Hence, there is no harm if there is a CP violation in the strong sector as long as we can find a plausible solution. On the contrary, a strong CP violation is directly connected to the existence of an electric dipole moment (EDM)  $d_n$  for a neutron. Experimentally, we have not found this to be the case in nature. Neutron does have a magnetic dipole moment, but the existence of an electric dipole moment would violate  $P$  and  $T$  symmetry. If  $T$  symmetry is broken, CP has to be violated as CPT needs to be conserved.

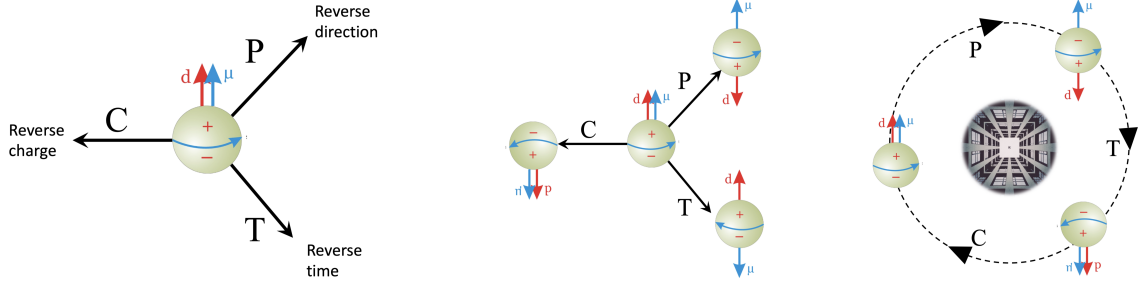


Figure 2.1: CPT transformations of a neutron. The figure is taken and modified from [16].

**Classical Interpretation** The existence of an electric dipole moment due to  $CP$  violation in the strong sector can be motivated in a classical setting [17]. In this picture, the neutron consists of three quarks (up, down, down). These quarks form a triangle, as seen in the left panel of fig.(2.2),

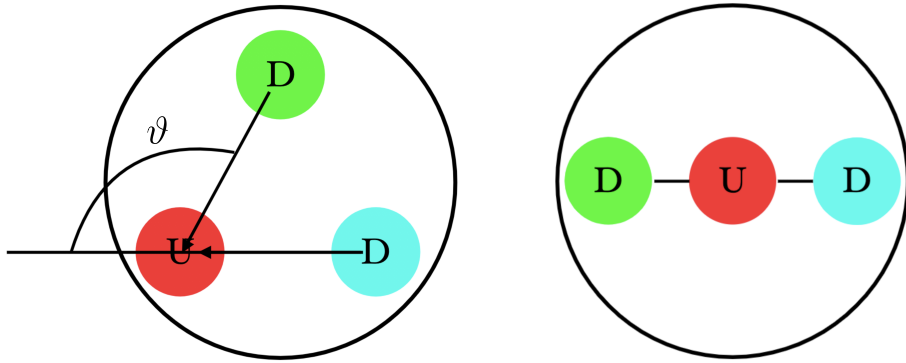


Figure 2.2: *Left:* A classical picture of the neutron ; *Right:* Axion solution to the Strong CP problem, a dynamical angle between the up and down quarks will be set such that the neutron relaxes itself to the minimum energy configuration without a dipole moment. This dynamic angle is called the axion. The figure is taken from [17].

We can estimate the value for the magnitude of neutron EDM for this classical model of a neutron using a classical picture where  $\vec{d}_n = \sum q\vec{r}$ . The direction of  $\vec{d}_n$  is the same as the direction of neutron spin (with a factor of +1 if parallel and -1 if anti-parallel). Each pair of quarks will contribute to the dipole moment as  $\sim er_n$ . We can use the fact that neutron has a size  $r_n \sim 1/m_\pi$ , we get

$$\left| d_n = \frac{er_n}{3} \right| \approx 10^{-13} \sqrt{1 - \cos \vartheta} e \text{ cm.} \quad (2.10)$$

From this calculation, we expect neutron EDM to be at the order of  $10^{-13} \text{ cm}$ . Until now, experiments have not been able to measure any EDM for the neutron,

giving an extremely tight bound of  $d_n < 10^{-26}e$  cm [17]. This implies that the angle  $\vartheta < 10^{-13}$ , which means that the three quarks should be collinear, as seen in the right panel of fig.(2.2). At its heart, the strong CP problem concerns why  $\vartheta < 10^{-13}$  is so small.

## 2.2 QCD Axion

The axion is one of the solutions to the strong CP problem proposed by Pecci and Quinn [1]. The gist of this solution is that we assume  $\bar{\theta}$  to be dynamic by letting  $\bar{\theta} \rightarrow \bar{\theta} + \frac{a}{f_a}$ .  $a$  is the axion field, and  $f_a$  is the axion decay constant. This means that our new field also couples to the gluon similar to the  $CP$ -symmetry breaking term,

$$\frac{g^2}{32\pi^2} \frac{a}{f_a} \tilde{G}_{\mu\nu}^a G^{\mu\nu a} \quad (2.11)$$

Then, we choose a minimized potential for  $\theta = 0$  and solve the problem dynamically.

To use the Pecci-Quinn mechanism, we begin by introducing a complex scalar field (also called the PQ field),

$$\Phi = \chi e^{i\phi} = \chi e^{i\frac{a}{f_a}}, \quad (2.12)$$

where we redefined the  $\phi$  field with  $a$ ,  $f_a$  is known as the axion decay constant, which ensures that the term in the exponent is dimensionless.

In the next step, we need to introduce an additional chiral  $U(1)$  symmetry - the  $U(1)_{\text{PQ}}$  symmetry for the  $\Phi$  field, known as the Pecci-Quinn symmetry. This is a global symmetry given by  $\Phi \rightarrow e^{i\alpha}\Phi$ , under which the theory remains invariant. With respect to the  $a$  field, this same symmetry translates into a shift symmetry  $a \rightarrow a + \alpha$ . The  $U(1)_{\text{PQ}}$  symmetry is spontaneously broken by the potential,

$$V(\Phi) = \lambda \left( |\Phi|^2 - \frac{f_a^2}{2} \right)^2, \quad (2.13)$$

to a non-zero vacuum expectation value of  $\Phi$  proportional to the decay constant  $f_a$ . The shape of this potential is similar to the Mexican hat potential (This is the same shape of the potential that introduces the Higgs boson in the electroweak theory via spontaneous symmetry breaking) like the top-hat (hat-shaped potential aligned on the top-left of the figure) in fig.(2.3). Goldstone's theorem says that breaking a continuous symmetry always results in a massless excitation, known as the Goldstone mode. The massless particle associated with this excitation is known as a Goldstone boson [18]. Then, if we consider QCD instanton effects, the potential energy gets a contribution

$$V(\Phi, \Phi^\dagger) \rightarrow V(\Phi, \Phi^\dagger) + \frac{m_\pi^2 f_\pi^2}{4} \frac{m_u m_d}{(m_u^2 + m_d^2)} \left[ 1 - \cos \left( \frac{a}{f_a} \right) \right], \quad (2.14)$$

such that it tilts the Mexican hat potential. This tilting provides the axion with its mass, like in the second and third step of the hat-shaped potential in fig.(2.3). This provides a mass to our originally massless particle, giving us the axion. In short, the axion is a pseudo-Nambu-Goldstone boson due to spontaneously broken  $U(1)_{PQ}$  in the presence of QCD instantons.

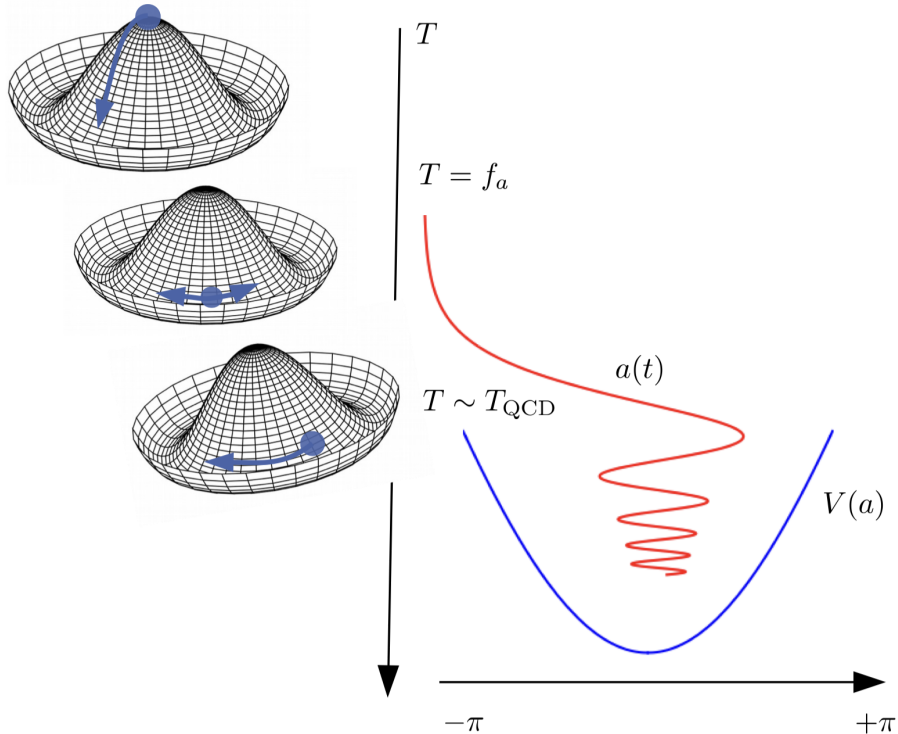


Figure 2.3: The Vacuum Realignment Mechanism. At temperatures  $T = f_a$ , the complex Peccei-Quinn scalar field develops its vacuum expectation value and breaks the global  $U(1)_{PQ}$  symmetry. The figure and its description is taken from [19].

The axion mass  $m_a$  can be calculated in chiral perturbation theory and at zero temperature is given by [20],

$$m_{a,\text{QCD}} \approx 6 \text{ }\mu\text{eV} \left( \frac{10^{12}}{f_a} \right). \quad (2.15)$$

At high temperatures, for example, above the QCD phase transition temperatures, the axion is massless [19]. In the original axion model proposed by Pecci-Quinn,  $f_a$  is taken to be the order of the electroweak (EW) breaking scale. This does not only lead to quite heavy axions,  $m_a \sim \text{keV}$ , but also sizable coupling to other standard model (SM) particles. The PQ axion model was ruled out by beam dump and other experimental constraints [19]. It has been found that the

essence of the PQ mechanism can still be retained while new degrees of freedom are added. This allows the symmetry breaking scale to go to higher energies, much greater than the EW symmetry breaking. There are two most prominent examples :

- DSFZ [21,22]: In addition to the second Higgs doublet  $\Phi$ , another complex SM singlet field is added.
- KSVZ [23,24]: In this model, additional heavy SM quarks are included.

Both of these models let  $f_a$  go to arbitrarily high scales, which makes the axion light  $m_a \sim \mu\text{eV}$  and very weakly interacting. These axion models are called invisible.

## 2.3 Axion Like Particles (ALPs)

An important model-independent feature of the PQ mechanism is that the axion always couples to the photon via,

$$\mathcal{L}_{A\gamma\gamma} = g_{A\gamma\gamma} \frac{\alpha}{2\pi} \frac{A}{f_A} F^{\mu\nu} \tilde{F}_{\mu\nu} = \frac{g}{4} A F^{\mu\nu} \tilde{F}_{\mu\nu}, \quad (2.16)$$

where  $A$  is the ALP (We use this notation just for this section to distinguish with  $a$  being the QCD axion. Except this section, we use  $a$  for any axions) and  $\alpha$  here is the fine structure constant. Using this coupling, one can consider a generic model where the axion mass is not set by QCD dynamics but instead due to some other UV effect. The spontaneously broken potential to give the axion mass looks similar to eq.(2.14) [19],

$$V_{\text{ALP}} \sim \Lambda^4 \left[ 1 - \cos \left( \frac{A}{f_A} \right) \right] \quad (2.17)$$

In such models, we have two free parameters  $m_a$  is also a free parameter along with  $g_{a\gamma\gamma} \sim f^{-1}$ , giving us two free parameters instead of one. The primary terms in the Lagrangian of such a model are,

$$\mathcal{L} = \frac{1}{2} (\partial_\mu a)^2 + \frac{1}{2} m_a^2 a + \frac{g_{a\gamma\gamma}}{4} F_{\mu\nu} \tilde{F}^{\mu\nu} + .. \quad (2.18)$$

The motivation for these particles comes from the fact that most experiments looking for ultralight axions are sensitive to the couplings of photons.

Such models, where the mass is not an artifact of QCD effects, are Axion-Like Particles (ALPs). As a rule of thumb, we will specifically use the term QCD axion if we are referring to the axion for which the properties are set by QCD dynamics and necessarily solve the strong CP problem.

It is also worth mentioning that string theory predicts many axions and ALPs to exist. The existence of these string theory axions is many times referred to as *axiverse* [25].

## 2.4 Axion Production: Misalignment Mechanism

In the early universe, we had temperatures  $T \gg f_a$ ; hence, the PQ symmetry was not broken. Once the temperature fell below the axion decay constant, the axion came into existence as a massless Goldstone boson. Further, once the QCD phase transition  $\Lambda_{\text{QCD}}$  happened, axions shift symmetry was broken, and non-perturbative effects started to contribute. The axion field was frozen to a constant value corresponding to the Hubble friction. Eventually, as the Hubble parameter fell below the axion mass, the axion field began damped oscillations around a CP-conserving value.

The Lagrangian for this system can be written down as follows,

$$\mathcal{L} = - \left[ \frac{1}{2} (\partial_\mu a)^2 + V(a) \right]. \quad (2.19)$$

where the potential can be written as

$$V(a) = m_a^2 f_a^2 \left[ 1 - \cos \left( \frac{a}{f_a} \right) \right], \quad (2.20)$$

from eq.(2.17). It is convenient to work with the dimensionless field  $\theta \equiv a(x)/f_a$ , giving us [19],

$$\mathcal{L} = f_a^2 \left[ -\frac{1}{2} (\partial_\mu \theta) (\partial^\mu \theta) - V(\theta) \right], \quad (2.21)$$

$$V(\theta) = m_a^2 f_a^2 (1 - \cos \theta), \quad (2.22)$$

We define the geometry of an expanding universe by the FLRW metric. Assuming a flat  $k = 0$  FLRW metric, we have the line element defined by

$$ds^2 = -dt^2 + R^2(t) d\vec{r}^2, \quad (2.23)$$

$$g^{\mu\nu} = \text{Diag}(1, -R^2(t), -R^2(t), -R^2(t)). \quad (2.24)$$

The action is given by,

$$\mathcal{A} = \int d^4x \sqrt{-g} \mathcal{L}_\theta. \quad (2.25)$$

By varying the  $\theta$  field, we expect the equation of motion to be of the form,

$$\square \theta + V'(\theta) = 0, \quad (2.26)$$

where  $\square$  is the d'Alembertian operator of a scalar field in a flat FLRW metric, i.e., a flat expanding universe. The exact equations of motion for this field are derived in appendix A. The equation of motion is given by eq.(A.24) (rewritten here for convenience),

$$\left( \partial_t^2 + 3H\partial_t - \frac{\nabla^2}{R^2} \right) \theta + m_a(t)^2 \sin \theta = 0. \quad (2.27)$$

In the case that inflation occurs after the PQ transition, the axion field is homog-

enized over large distances; hence, we can ignore the spatial derivatives in eq. (2.27). For small  $\theta$ , we can further approximate the equation as follows,

$$\ddot{\theta} + 3H\dot{\theta} + m_a(t)^2\theta = 0. \quad (2.28)$$

This is the equation for a damped harmonic oscillator, where the friction is proportional to the Hubble parameter. We will call the term the *Hubble friction* parameter.

We can solve this ODE by assuming  $H = c/t$ , where  $t$  is the time, and  $c$  is a constant. For the initial conditions, we assume that  $H \gg m_a$  at very early times. This makes the axion field overdamped and the term with the time derivative vanishes,

$$a(t_i) = a_i, \quad \dot{a}(t_i) = 0. \quad (2.29)$$

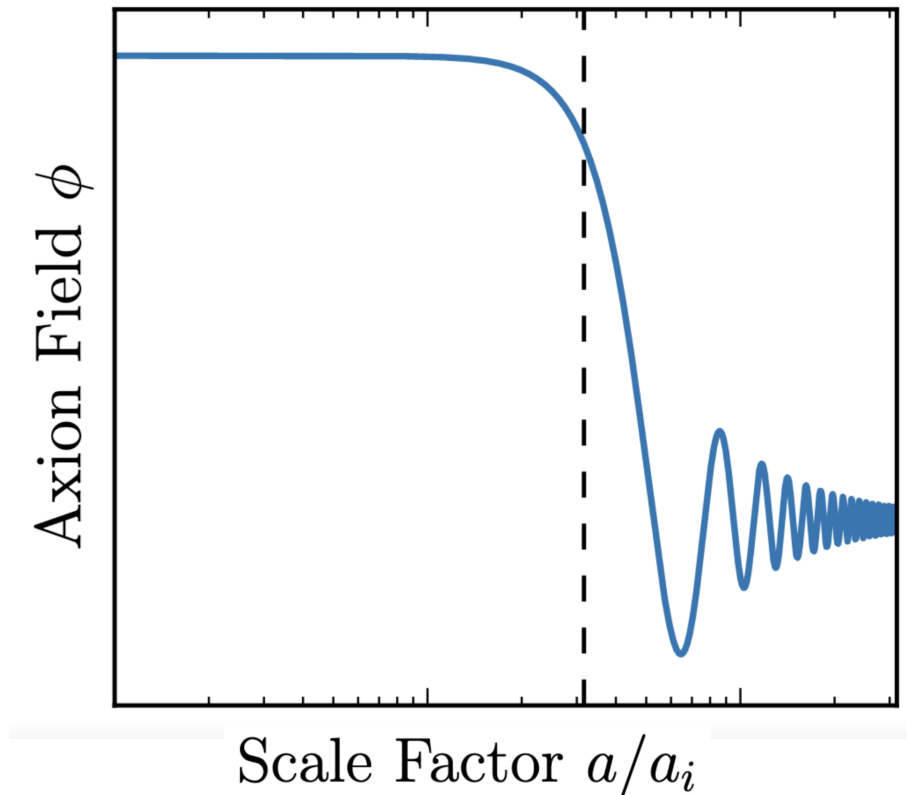


Figure 2.4: Evolution of axion ( $\phi \rightarrow \theta$  in our calculation) quantities in the exact solution to the background evolution of an ALP for a radiation-dominated universe. The figure and its description is taken from [20].

In fig.(2.4), we can see that the axion field is initially frozen, and at a certain point, it starts damped oscillations as expected from the equation of motion.

## 2.5 ALP Dark matter

This section briefly discusses the candidacy of axions or ALPs as Dark Matter (DM). Simply speaking, we need three conditions that any dark matter candidate needs to satisfy [26] :

1. **Relic Density:** Any relevant DM theory must give us the predicted DM density. A detailed calculation showing that zero-momentum modes of ALP's have a temperature-independent mass (from the misalignment mechanism) and satisfy the observed relic density is found in [27].
2. **Weak Interactions with SM:** Particle DM candidates must be extremely weakly coupled to Standard Model (SM) particles. Axions are produced due to anomalies and are very weakly coupled to SM particles. Axions can decay into photons (In fact, this is the same interaction we will be probing extensively in this thesis). The decay occurs due to a Chiral anomaly [10], and substituting the current upper limit parameters for their coupling constant and mass gives us their lifetime much longer than the age of the universe [12].
3. **Structure formation:** DM candidates need to be able to form structure to account for observational evidence. Although axions are very light, they can form cold dark matter (CDM) via the misalignment mechanism. One proposed idea is that they form a Bose-Einstein condensate, thus enabling them to create structures [6].

## 2.6 Axion Searches

### 2.6.1 Detection principle

As seen before, axion couples to the photon via the  $a\gamma\gamma$  vertex. Most experimental searches utilize this coupling as an attempt to detect axions. The vertex is given by the following term in the Lagrangian,

$$\mathcal{L} \supset g_{a\gamma\gamma} a F \tilde{F} = -4g_{a\gamma\gamma} a \vec{E} \cdot \vec{B}. \quad (2.30)$$

When a high-energy photon interacts with the photon coming from an electromagnetic field, it can produce an axion. This is known as the axion Primakoff-effect. This process suggests that objects with a high density of energetic photons in an external electromagnetic field (like dense nuclear medium or plasma) are potentially strong axion sources. Stars, supernovae, and neutron stars satisfy these conditions, making them axion emitters. Similarly, the inverse Primakoff-effect is when an axion decays into photons in a strong magnetic field. The inverse Primakoff effect is one of the core principles used in indirect detection experiments. The starting point for computing the probability rates of axion-photon conversion is the Axion-Maxwell equations, also known as equations

for axio-electrodynamics in literature. The derivation of these equations can be found in appendix B. In articles [28, 29], one can find a reasonably exhaustive and (nearly) up-to-date review of various experiments looking for axions.

## 2.6.2 Haloscopes

When experiments focus on detecting axion dark matter, they are known as Haloscopes (named after the fact that we expect to find dark matter in Halos). The earliest mention of haloscopes can be found in [2–4]. These are the same articles that were among the first to explore the detection possibility of an "invisible" axion by exploiting its interaction with the electromagnetic field.

The primary goal of haloscopes is to detect axions from the Milky Way's dark matter halo. The number density of these particles is quite low (even assuming we have a purely axionic halo). A conceptual setup of an experiment designed to detect DM axions is shown in fig. (2.5). In such a setup, as the axions enter the cavity, they can be converted to photons due to the magnetic field. Using this, we can find a resonance in the frequency, enabling us to determine the mass of the observed particle.

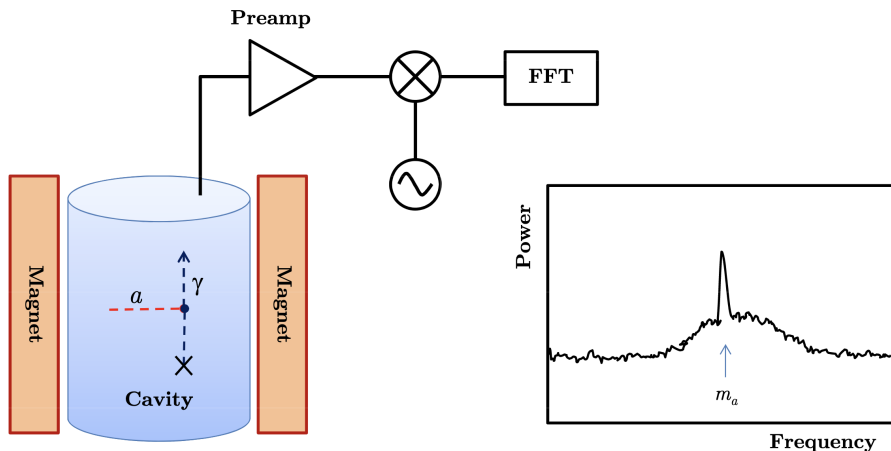


Figure 2.5: Schematic of a Haloscope. The figure is taken from [28].

The ADMX (Axion Dark Matter eXperiment) [30] is the only current experiment that looks for plausible detection of axionic dark matter. The sensitivity of this experiment goes to axion masses in the few  $\mu\text{eV}$  range. Unfortunately, it has not detected any signal but has excluded a good amount of parameter space which can be seen in fig.(2.6).

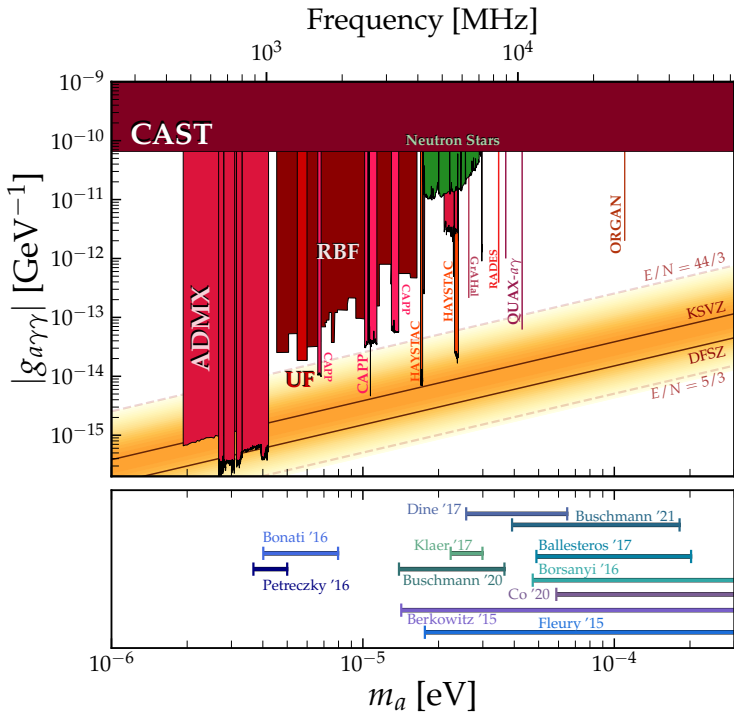


Figure 2.6: Axion-Photon coupling parameter space, zoomed in on Haloscope bounds. The figure is taken from [31].

Another promising experiment proposed in recent years is from the MADMAX (MAgnitized Disk and Mirror Axion eXperiment) collaboration [32]. This experiment proposes to detect dark matter axions in the mass range of 40-400  $\mu\text{eV}$  by placing dielectric disks in a magnetic field. These setups are called *dielectric haloscopes*, a schematic of such a setup can be seen in fig.(2.7)

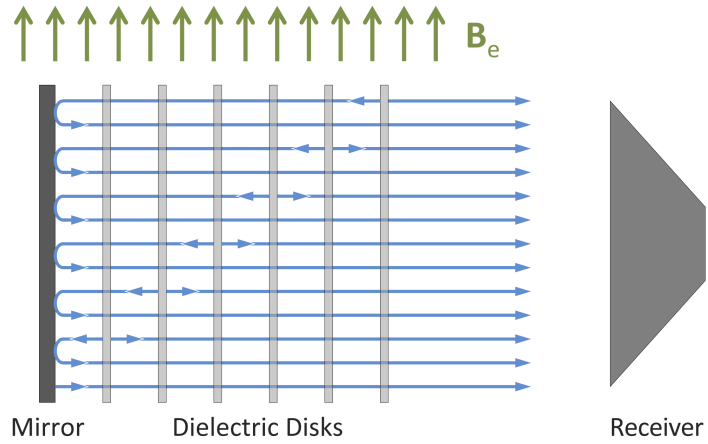


Figure 2.7: Schematic of a dielectric haloscope. The figure is taken from [33].

### 2.6.3 Light Shining Through Walls (LSW) experiments

An important axion detection experiment is called the "Light Shining Through Walls" (LSW). In such experiments, powerful lasers are used as an axion source. The idea is as follows: A powerful laser is shined inside a strong magnetic field, so a part of the beam converts to axions. Then, a wall is placed in the path of a beam so that none of the photons but all axions can pass through it. Then, the axions that pass through the walls are passed through another powerful magnetic field, partially converting them into photons. If any such photons are detected on the other side of the partition, then all of these photons need to be an artifact of axions converting back to photons in the presence of the magnetic field. A schematic of such experiments is shown in fig.(2.8).

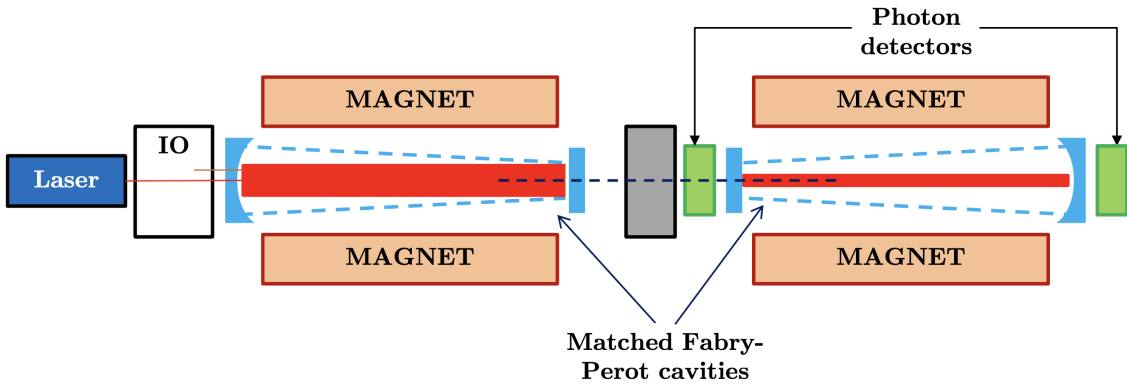


Figure 2.8: Schematic of an LSW experiment. The figure is taken from [28].

Such an event has not been detected yet, giving strong upper bounds on the  $g_{a\gamma\gamma} < 10^{-8}$  GeV. As of now, LSW experiments are unable to probe the QCD axion. The parameter space for LSW experiments can be seen in fig.(2.9).

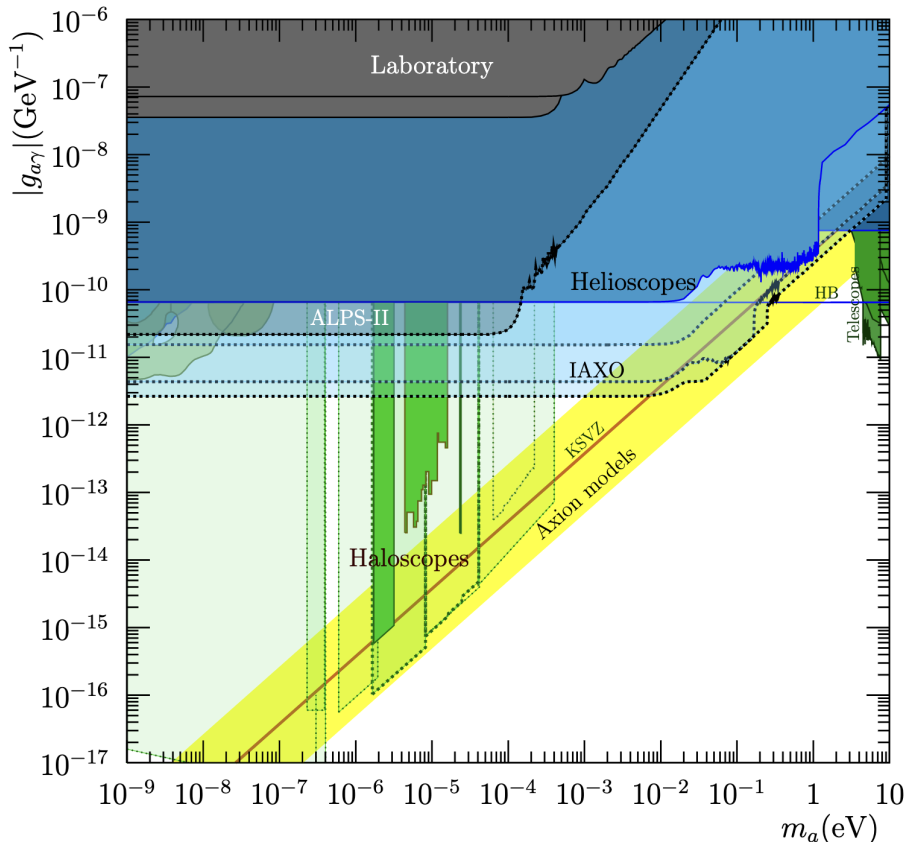


Figure 2.9: Excluded parameter space for axion-photon coupling from Haloscopes, Helioscopes, and LSW experiments. The figure is taken from [28].

#### 2.6.4 Helioscopes

When axion detection experiments concern the detection of solar axions and ALPs, these searches are called axion helioscopes (derived from the word *Helios*, the ancient Greek word for Sun). Like LSW experiments, ALPs are converted into photons under a strong magnetic field. Since only one conversion occurs in helioscopes, they can search for ALPs with weaker couplings. A schematic of such searches can be seen in fig.(2.10). The parameter range already excluded by helioscopes can also be seen in fig.(2.9). Future planned helioscopes can test parts of the QCD axion parameter range.

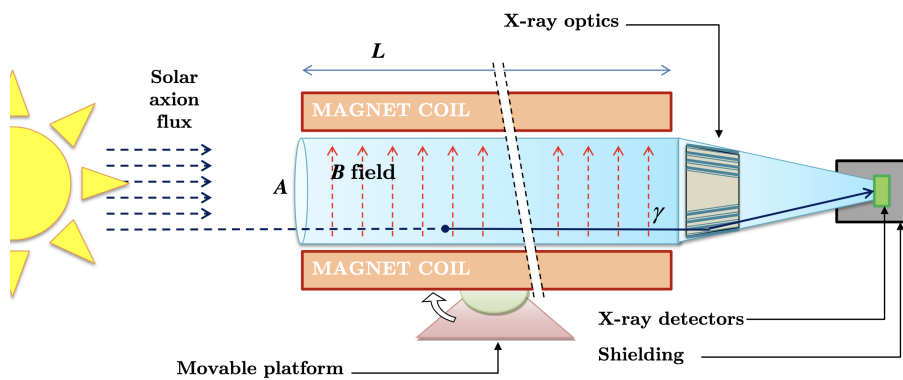


Figure 2.10: Schematic of a Helioscope experiment. The figure is taken from [28].

# Chapter 3

## Production of axion echo

In article [11], the authors propose sending out a powerful beam of microwave radiation into a region in space where we expect an excellent dark matter density. The purpose of this signal is to listen to a potential echo by stimulating the axionic dark matter halo and listening to its echo to detect axion dark matter. We call the back-decayed signal from such an echo axion gegenschein, and the forward-decayed signal is called axion forwardschein (In contrast to the literature, where an axion echo corresponds to a gegenschein signal).

Similar to this idea, several studies like [13, 14, 34] have proposed unique ways to detect the echo. Instead of sending out a powerful radiation beam, these studies suggest searching the echo using astrophysical sources that will be the source providing the electromagnetic signal necessary for the enhanced decay.

### 3.1 Axion echo from a point source

We take a limit where the axion has a high occupation number. In this scenario, we can compute the gegenschein intensity by solving the classical field equations for an axion coupled to the photon [13]. We have a perfectly cold axion fluid density given by  $\rho$ . Let  $P_0$  be the power of the electromagnetic wave that enters this density and produces the axion echo. The power of echo signal  $P_1$  is given by (in natural units),

$$P_1 = \frac{g^2 \rho}{16} \left[ \frac{dP_0}{d\omega} \right]_{\omega=\frac{m_a}{2}} \pi t \quad (3.1)$$

which is derived in its full glory in appendix C following [11].

The physical process is such that we get a significant stimulated decay when the angular frequency of the radiation  $\omega_d$  is equal to half the axion mass  $m_a$  (in natural units),

$$\omega_d = \frac{m_a}{2} \quad (3.2)$$

In SI units, we can deduce the relationship between the frequency of the

photon  $\nu_d$  and the mass of the axion,

$$h\nu_d = \frac{m_a c^2}{2} \quad (3.3)$$

An alternative formulation of eq.(3.1) is given by,

$$S_g = \frac{\hbar c^4}{16} (g_{a\gamma\gamma})^2 S_\nu (\nu_d) \int dx \rho_a [r(x)]. \quad (3.4)$$

$S_g$  is the gegenschein flux density,  $S_\nu (\nu_d)$  is the specific flux density of the source at frequency  $\nu_d = m_a / 4\pi$  and the integral is along the axion density [13,34]. To compute the forwardschein signal, we choose the axion density column integral appropriate to the scenario. We will refer to eq.(3.4) as the "central formula" multiple times to estimate the flux density of axion echo signals.

## 3.2 Stimulated emission of axions in a photon bath

In the article [12], the authors compute an enhanced photon signal from an axion density profile due to Bose enhancement. This independent calculation advocates for stimulated axion decay in the presence of photons. Hence, we briefly summarize the idea and the main results here.

The decay of an axion with mass  $m_a$  takes place through the Chiral anomaly and produces two photons, each with frequency  $\nu = m_a / 4\pi$ . One can express the lifetime of the axion in terms of its mass and its effective two-photon coupling  $g_{a\gamma\gamma}$

$$\tau_a = \frac{64\pi}{m_a^3 g_{a\gamma\gamma}^2} \quad (3.5)$$

Evaluating this value for  $m_a \sim 1 \mu\text{eV}$  and coupling near the upper limit  $g_{a\gamma\gamma} \sim 10^{-10} \text{ eV}$  gives us  $\tau \sim 10^{32} \text{ years}$ . However, this is a decay rate only valid in a vacuum. Suppose we assume the axion decay takes place inside a radiation field. In that case, the photon production rate will be enhanced by stimulated emission - a phenomenon because photons are indistinguishable and follow Bose-Einstein statistics. The article calculates the stimulated emission of axion into two photons. The Boltzmann equation for such a process leads to the following result,

$$\dot{n}_a \simeq -n_a \Gamma_a (1 + 2f_\gamma) \quad (3.6)$$

where  $n_a$  is the number density of axions,  $\Gamma_a$  is the decay rate of axions, and  $f_\gamma$  is the occupation number of photons. This result is valid in the limit  $f_a \gg f_\gamma$ . This means that the effect of stimulated emission can be incorporated by multiplying the spontaneous emission rate by a factor of  $2f_\gamma$  in this limit.

# Chapter 4

## Stellar Basins

This chapter is an executive summary of the relevant sections needed from article [9] for the thesis. Hence, several statements in this section are directly borrowed from [9]. We have elaborated the arguments and calculations to various degrees of freedom whenever possible.

In article [9], the author hypothesizes a novel physical phenomenon, which he summarizes using the following line, "stars can emit massive particles into bound orbits." Specifically, stellar-produced weakly coupled particles like axions can enter gravitationally bound orbits around them (depending on their velocities). While most of the emitted particles are relativistic, a small part of the phase space allows a tiny fraction of these particles to be bound in these orbits. This tiny fraction of particles accumulate over the astrophysically large time scales, effectively forming what the author calls a "Stellar Basin". The author finds that after a million years, for any sufficiently long-lived particle (produced through an emission process whose matrix elements are unsuppressed at low momentum), the energy density of the solar basin of such a particle will surpass the energy density of the relativistic solar flux. The mere existence of such basins enhances the success rate of direct and indirect detection searches, helping us further constrain the parameter space of the respective basin particle. Following the original article, we will motivate, calculate and summarize the main results of our interest in forming a basin of solar axions. For convenience, we will break our calculation into multiple parts, like in the original paper. As an interesting side note, an earlier mention of gravitationally trapped ALPs accumulating over cosmic times is discussed in article [35].

A similar calculation for dark photon basins is done in article [36]. Further developments looking for indirect detection constraints on  $g_{a\gamma\gamma}$  from the Solar axion basin are done in [37]. An innovative and interesting calculation approach in computing the basin of gravitationally bound millicharged particles (MCPs) is taken in [38]. Following a different production channel for axions based on the Axion Quark Nugget (AQN) dark matter model [39,40], article [41] discusses

the possibility of gravitationally trapped axions on Earth.

## 4.1 Idea : Basin Formation

We start by assuming a volumetric-emission process of a weakly interacting particle with mass  $m$  and  $dQ/d\omega$  as the differential energy loss rate per unit volume per energy. The energy of the emitted particle is given by the famous  $\omega = \sqrt{m^2 + \vec{k}^2}$  relation. Note that the stellar photon emission process is not volumetric but only through the Star's surface, which makes the sun a poor photon emitter (in comparison to the particle/s we are considering). Suppose  $dQ/d\omega$  as a function of  $\omega$  in an analytic form or as a dataset is known; the total luminosity for such a process will be given by taking a volume integral over the stellar interior,

$$L = \int d^3R' \int_m^\infty d\omega \frac{dQ}{d\omega}. \quad (4.1)$$

Here, we take a toy model to illustrate our point (same toy model as in the paper) as shown in fig.(4.1). The plot shows a differential energy loss rate per unit volume per energy as an energy function. The solid black line in the figure corresponds to the  $dQ/d\omega$  rate for a particle of mass  $m$ . We are particularly interested in the blue sliver in the figure. The blue sliver corresponds to  $m < \omega < m(1 + v_{\text{esc}}^2/2)$ , which means that the particle has just enough energy to be produced, but not enough to overcome the escape velocity of the Sun. In general stellar energy loss calculations, one computes the integral under the whole curve; such techniques are used to set stellar cooling constraints on coupling constants for various BSM particles.

Although these particles ( $\omega \approx m, |\vec{k}| \ll m$ ) contribute to a tiny fraction of the luminosity, they are the same ones with a high probability of ending up in bound orbits.

## 4.2 Calculation : Basin Formation

In this section, we will derive the density of such a basin of particles.

For convenience, we will define a variable  $\tilde{\omega}_k$  which denotes *kinetic energy per unit mass* in the following way,

$$\tilde{\omega}_{\text{kin}} \equiv \frac{\omega_{\text{kin}}}{m} = \frac{\omega - m}{m} \approx \frac{\vec{k}^2}{2m^2}. \quad (4.2)$$

The last approximation comes from the fact that we can safely assume particles in bound orbits will have non-relativistic velocities, giving us  $\omega_{\text{kin}} = \vec{k}^2/(2m)$ .

For the particles to end up in the basin, we need that the following quantity is asymptotically negative,  $\tilde{E} \equiv \tilde{\omega}_{\text{kin}} + \Phi(R)$ ,

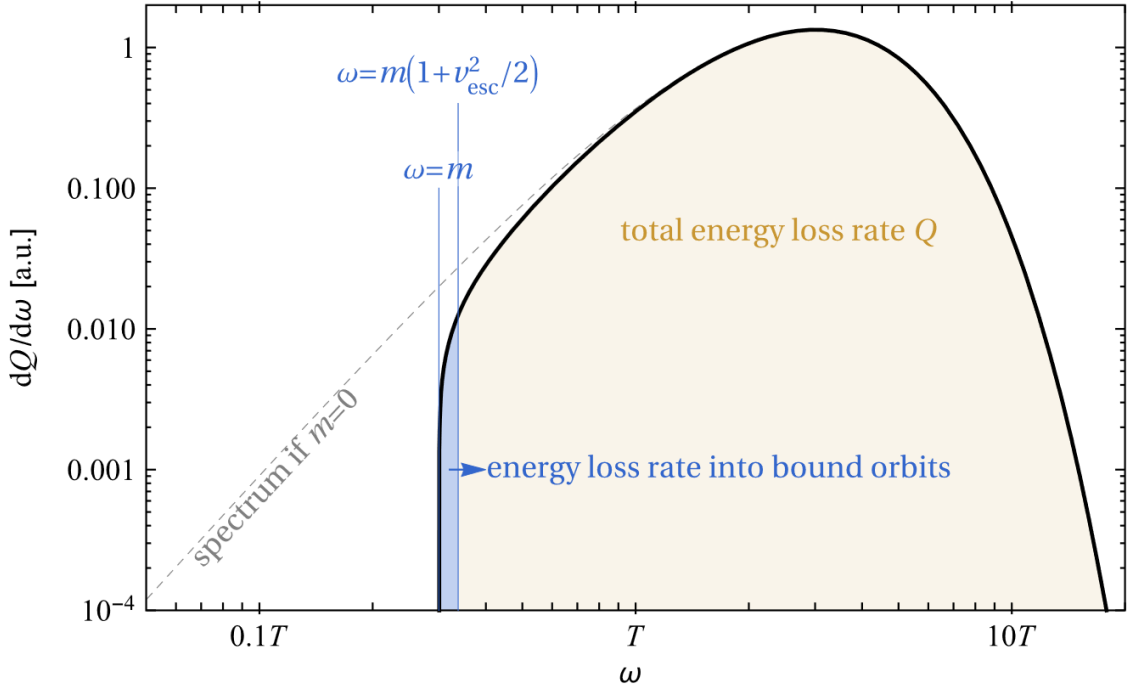


Figure 4.1: Black curve: A generic differential energy loss rate per unit volume  $dQ/d\omega$  per energy  $\omega$  of the emitted particle. The blue sliver represents the nonrelativistic modes gravitationally bound to the star. The figure and its description is taken from [9].

where  $\tilde{E}$  is the energy per unit mass, and  $\Phi$  is the gravitational potential. The condition  $\tilde{E} < 0$  gives us  $\tilde{\omega}_{\text{kin}} < \Phi$ , meaning that the particle doesn't have enough kinetic energy to escape from the gravitational potential (everything here is classical, the only difference being, we are working in *energy per unit mass* variables).

The next logical step is to compute  $\mathcal{P}(R, \tilde{E})$ , which is the probability density that a particle with energy  $\tilde{E}$  is found at a radius  $R$ . From classical mechanics, we expect that this quantity is inversely proportional to,

1. The velocity of the particle, which can be written as

$$v(R, \tilde{E}) = \sqrt{2[\tilde{E} - \Phi(R)]}. \quad (4.4)$$

Higher velocities make it less likely for a particle to be found at a radius of  $R$ .

2. The square distance  $R^2$ . This comes from Gauss's law. The larger the radius, the larger the surface area of the shell. This contributes to a lower probability of finding a particle at  $R$ .

This gives the following form for our probability density,

$$\mathcal{P}(R, \tilde{E}) = \frac{C(\tilde{E})}{R^2 v(R, \tilde{E})}, \quad (4.5)$$

where  $C(\tilde{E})$  is a normalization constant. This constant is fixed by requiring the normalization condition  $\int d^3R \mathcal{P}(R, \tilde{E}) = 1$ . For a gravitational potential of the form  $\Phi(R) \simeq -GM_*/R$ , one finds the following form for the constant,

$$C(\tilde{E}) \simeq \frac{1}{\sqrt{2\pi}} \frac{(-\tilde{E})^{\frac{3}{2}}}{GM_*}. \quad (4.6)$$

This formalism is a good approximation for particles having orbits  $R \gg R_*$ , where  $R_*$  is the radius of the stellar body around which the basin is being formed.

We can now define the injection rate at which the particles enter bound orbits, populating the basin. We define the injection rate in terms of the bound energy density. At  $R \geq R_*$  the bound energy injection rate is given by the following expression,

$$\dot{\rho}_{\text{bound}}(R) = \int d^3R' \int_{\Phi(R)}^0 d\tilde{E} \frac{dQ}{d\tilde{\omega}_k} \mathcal{P}(R, \tilde{E}). \quad (4.7)$$

Eq.(4.7) comes from the fact that the energy density injection rate is equal to the volumetric integral over the interior of our stellar body, integrated over all the possible bound energies (of the differential energy loss rate), times the probability density  $\mathcal{P}$  defined in eq.(4.5) and (4.6).

In order to make any further estimate on  $\rho_{\text{bound}}$  we need an expression for  $dQ/d\tilde{\omega}_k$ . By definition, this term depends on the process we are considering. Although, there is enough evidence in literature such that we could generalize this term to leading order in series as,

$$\frac{dQ}{d\tilde{\omega}_k} = \sum_p \tilde{Q}_p(R') \tilde{\omega}_k^{n_p/2} \quad (4.8)$$

where  $n_p \in \mathbb{Z}^+$ , the sum over  $p$  makes sure that you include all the production processes for the particle in interest contributing to the term,  $\tilde{Q}_p$  is used to extract the energy dependence such that it only depends on the stellar interior radius  $R' < R_*$  (where a spherical symmetry has been assumed for the system). To motivate eq.(4.8), we can look at a quick generic example where the matrix element remains constant in the soft limit, i.e.  $|\mathcal{M}|^2 \simeq \text{const}$  as  $\vec{k} \rightarrow 0$ . The main purpose of this illustration is to see that for such a process; one can reach the form of eq.(4.8) when  $n_p = 1$ . As we are assuming a constant matrix element, a good starting point is to see how the integral over momentum fares,

$$\int \frac{d^3k}{(2\pi)^3} = \frac{1}{(2\pi)^3} \int k^2 dk d\Omega = \frac{4\pi}{(2\pi)^3} \int k (dk). \quad (4.9)$$

We want to make a change of variables from  $k \rightarrow \tilde{\omega}_k$ . We can start from the non-relativistic approximation for  $\tilde{\omega}_k$ ,

$$\tilde{\omega}_k = \frac{k^2}{2m^2} \quad (4.10)$$

$$k = \sqrt{2\tilde{\omega}_k m^2}, \quad (4.11)$$

and

$$\frac{d\tilde{\omega}_k}{dk} = \frac{k}{m^2} \quad (4.12)$$

$$k dk = m^2 d\tilde{\omega}_k, \quad (4.13)$$

which we can plug into eq.(4.9) to get,

$$\int \frac{d^3 k}{(2\pi)^3} = \frac{1}{2\pi^2} \int \sqrt{2\tilde{\omega}_k m^2} m^2 d\tilde{\omega}_k \quad (4.14)$$

$$= \frac{m^3}{\sqrt{2}\pi^2} \int \sqrt{\omega_k} d\tilde{\omega}_k. \quad (4.15)$$

From here, we can see that such processes give rates equivalent to eq.(4.8) for  $n_p = 1$ . We will see later that these  $n_p = 1$  processes fill the stellar basin effectively.

Now, we will plug in eq.(4.4), (4.5), and (4.8), in eq. (4.7), which give us the following expression for the bound energy density injection rate (at  $R \geq R_*$ ),

$$\dot{\rho}_{\text{bound}}(R) = \sum_p \int d^3 R' \int_{\Phi(R)}^0 d\tilde{E} \frac{\tilde{Q}_p(R')}{R^2} \frac{C(\tilde{E})}{\sqrt{2}} \frac{[\tilde{E} - \Phi(R')]^{\frac{n_p}{2}}}{[\tilde{E} - \Phi(R)]^{\frac{1}{2}}}. \quad (4.16)$$

We can safely approximate  $\tilde{E} - \Phi(R') \simeq -\Phi(R')$  when  $R \gg R_*$  (where  $R_* = \max R'$ ). Plugging in eq.(4.6) with this approximation, we can derive the bound energy injection rate,

$$\dot{\rho}_{\text{bound}} = \frac{1}{2\pi^2 R^2 GM_*} \sum_p \int d^3 R' \tilde{Q}_p(R') |\Phi(R')|^{\frac{n_p}{2}} \int_{\Phi(R)}^0 d\tilde{E} \frac{(-\tilde{E})^{\frac{3}{2}}}{[\tilde{E} - \Phi(R)]^{\frac{1}{2}}}, \quad (4.17)$$

where the integral over  $\tilde{E}$  converges if  $\Phi(R) < 0$ . Plugging in the result of the integral and substituting  $\Phi(R) \simeq GM_*/R$  (which satisfies  $\Phi(R) < 0$ ), we get the final equation,

$$\boxed{\dot{\rho}_{\text{bound}}(R) = \frac{3}{16\pi} \frac{GM_*}{R^4} \int d^3 R' \sum_p \tilde{Q}_p(R') |\Phi(R')|^{\frac{n_p}{2}}.} \quad (4.18)$$

Apart from the emission process itself, we can see that the bound energy injection rate drops as  $R^4$ . We will use this fact multiple times in the chapter 5 when the axion basin density is used to compute prospective detection rates

from basins of various compact stellar objects.

### 4.3 Solar Axion Basin

We have established a generic formalism to form stellar basins in section 4.2. Using that formalism, we compute the stellar axion basin for our sun in the following section. The result of this section is fig.(4.4), which is extremely crucial for chapter 5. Again, following the original article [9], we will compute the basin density for axions produced by the sun using axion-bremsstrahlung and axion-Compton emission processes.

For a general emission process of a weakly coupled boson with four-momentum  $k = (\omega, \vec{k})$ , the net energy loss rate per unit volume is,

$$Q = \frac{1}{(2\pi)^3} \int \frac{d^3 k}{2} \int dP_{in} \int dP_{out} |\bar{\mathcal{M}}|^2 (2\pi)^4 \delta^4 (P_{in} - P_{out} - k) \mathbb{F}. \quad (4.19)$$

Using the above equation, we want to compute  $\tilde{Q}_p$ , where  $p$  stands for the process. We do this by massaging eq.(4.19) for different processes into eq.(4.8). This enables us to substitute  $\tilde{Q}_p$  for a process  $p$  into eq.(4.18) computes the bound energy injection rate.

#### 4.3.1 Process 1 : Axion-Bremsstrahlung

Fig.(4.2) sketches the Feynman diagram for axion bremsstrahlung,

$$e^- (p_1) + Z_j (p_2) \rightarrow e^- (p_3) + Z_j (p_4) + a(k). \quad (4.20)$$

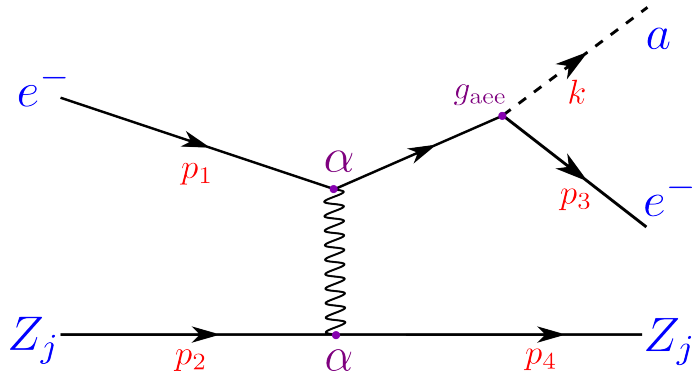


Figure 4.2: Feynman diagram for Axion-Bremsstrahlung.

The production results from electron collisions with nuclear ions of charges  $Z_j$  and masses  $m_j$ . The squared matrix element in the soft limit is given by,

$$|\bar{\mathcal{M}}_{B,j}|^2 = \frac{Z_j^2 e^4 g_{aee}^2}{\vec{q}^2 + \kappa_s^2} \frac{4m_j^2}{m_e^2} \quad (4.21)$$

where the  $\kappa = 4\pi\alpha(\bar{n}_N + n_e)/T$  term accounts for the screening effects (Debye Hueckel scale).  $\vec{q} \equiv \vec{p}_2 - \vec{p}_4$  takes care of the momentum transfer. We can make the following approximations,

- In stars like our Sun, the occupation of ions is low  $f_2, f_4 \ll 1$ .
- The ions are considered extremely heavy compared to the electrons, using which we can ignore any nuclear recoil.

Finally, plugging our matrix element into eq.(4.19) and after simplifying (entire simplification calculation is done in appendix D - we get an answer up to a factor of four compared to the author's result), this integral looks like the following (we use the author's results),

$$\frac{dQ_B}{d^3k} = \frac{\bar{n}_N e^4 g_{aee}}{256\pi^6 m_e^2} \int_m^\infty d\omega_p f_1(1-f_3) \ln \left( \frac{2+2\sqrt{1-\epsilon}-\epsilon+\xi}{\epsilon+\xi} \right). \quad (4.22)$$

In the above equation,  $\omega_p \equiv \vec{p}_1^2/2m_e$  is the kinetic energy of the incoming electron.  $\epsilon \equiv m/\omega_p$  is the ratio of the axion mass over the available kinetic energy in the electron. Finally,  $\xi := \kappa_s^2/2m_e\omega_p$  is a dimensionless screening measure.

At this point, we can consider two conditions. When the electrons are degenerate and non-degenerate. In the solar plasma, the electrons are degenerate as  $n_e \ll (m_e T)^{\frac{3}{2}}$ . This means we can safely ignore Pauli blocking. We can approximate this to  $f_3 \simeq 0$ . This means the only distribution factor that contributes in eq.(4.22) is  $f_1(\vec{p}_1)$ . Under these conditions specified, we can approximate  $f_1(\vec{p}_1)$  by a Maxwell-Boltzmann distribution,

$$f_1(\vec{p}) \simeq n_e \left( \frac{2\pi}{m_e T} \right)^{\frac{3}{2}} e^{-\omega_p/T}. \quad (4.23)$$

After converting from a  $\vec{k}$  integral to  $\tilde{\omega}$  integral using eq.(4.15) and using  $f_1(\vec{p})$ , we get an expression in the form of eq.(4.8) where,

$$\tilde{Q}_B \simeq \frac{\alpha^2 g_{aee}^2}{2\pi^{3/2}} \frac{\bar{n}_N n_e m^3}{m_e^{7/2} T^{1/2}} \int_0^1 d\epsilon \frac{\ln \frac{2+2\sqrt{1-\epsilon}-\epsilon+\xi}{\epsilon+\xi}}{\exp \left\{ \frac{m}{\epsilon T} \right\}}. \quad (4.24)$$

The integral can be evaluated numerically (or an alternative empirical formula is provided in [9]). An important point to emphasize is that another similar channel that could produce axions is given by axion-electron bremsstrahlung. The result is the same as axion-ion bremsstrahlung when  $\bar{n}_N \rightarrow n_e/\sqrt{2}$  [42].

Finally, one can compute the volume integral over a standard solar model (author uses the solar model from [43]), by substituting  $\tilde{Q}_B$  from eq.(4.24) into eq.(4.18). Golden curves in fig.(4.4) correspond to the contribution of electron-

ion bremsstrahlung to the local axion basin energy density  $\rho$  as a function of the mass of the axion (The volumetric integral depends on chosen axion mass).

### 4.3.2 Process 2 : Axion-Compton scattering

If we consider higher axion masses, i.e., significantly above the temperature (and plasma frequency of the sun), the axion-Compton process

$$\gamma(p_\gamma) + e^-(p_1) \rightarrow e^-(p_2) + a(k) \quad (4.25)$$

as shown in fig.(4.3) is the dominant axion production channel.

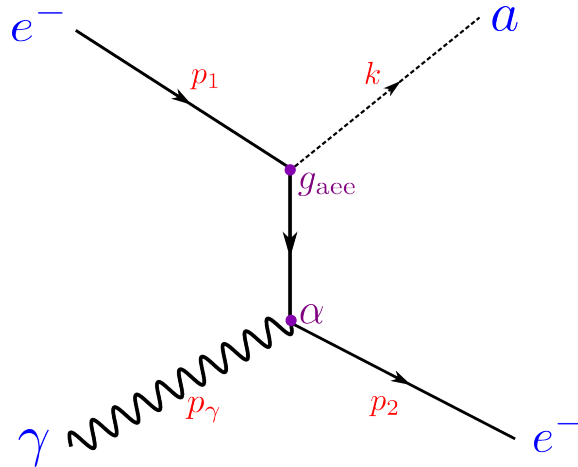


Figure 4.3: Feynman diagram for axion-Compton scattering process.

For the axion-Compton process, the squared matrix element in the soft limit is given by,

$$|\mathcal{M}_C| \simeq \frac{e^2 g_{aee}^2 m^2}{m_e^2}. \quad (4.26)$$

Similar to calculation of  $\tilde{Q}_B$  in section 4.3.1 and computation in appendix D, the author finds,

$$\tilde{Q}_c \simeq \frac{\alpha g_{aee}^2 n_e}{2^{\frac{2}{3}} \pi^2} \frac{m^5}{m_e^4} \frac{\sqrt{m^2 - \omega_{pl}^2}}{e^{\frac{m}{T}-1}} \quad (4.27)$$

where the variables correspond to the same quantities as in the case for axion-bremsstrahlung.  $\omega_{pl} = 4\pi\alpha n_e/m_e$  corresponds to the plasma frequency such that  $E_\gamma = \omega_{pl}^2 + p_\gamma^2$ . This process is kinematically allowed only when  $m > \omega_{pl}$ . Plugging eq.(4.27) into eq.(4.18) and computing the integral over the standard solar model, we get the red curves corresponding to the contribution of axion-Compton processes to the local axion basin energy density.

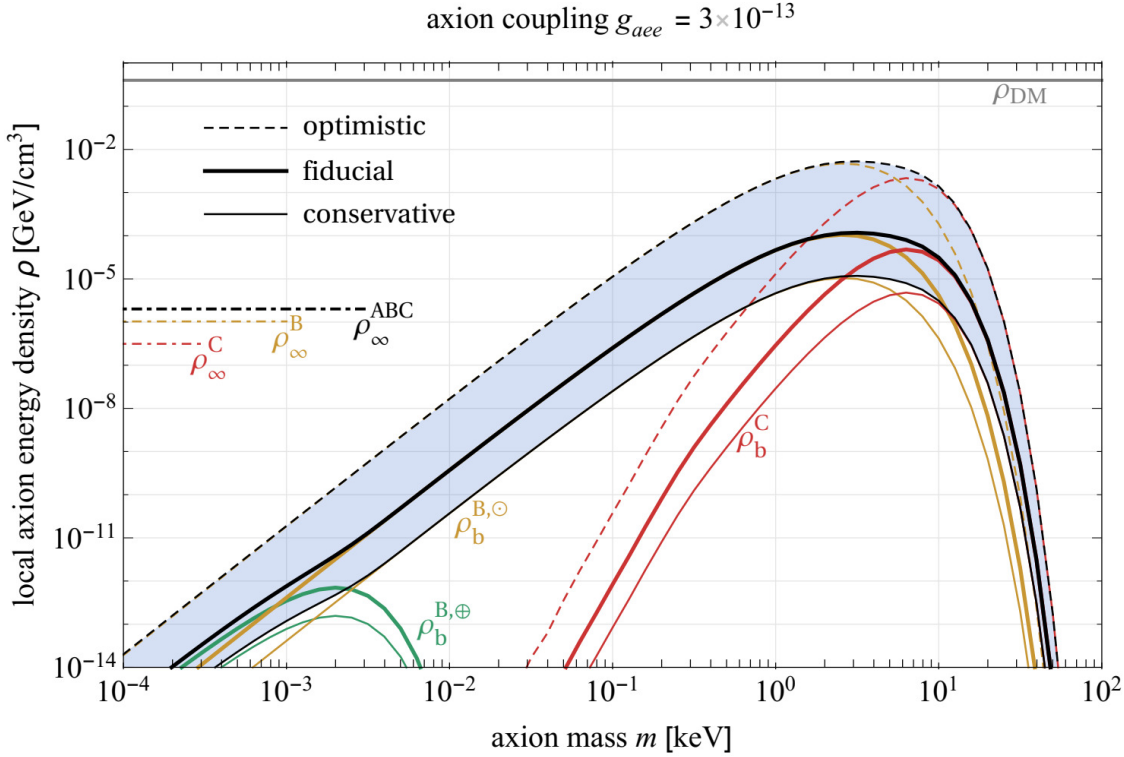


Figure 4.4: Axion energy density at Earth's surface from the solar basin denoted  $\rho_b$ , plotted as a function of axion mass  $m$ , and  $g_{aee} = 3 \times 10^{-13}$ . The relativistic solar flux is denoted by  $\rho_\infty$ . The axion energy density is plotted for conservative, fiducial and optimistic basin lifetimes corresponding to  $10^7, 10^8$  and  $4.5 \times 10^9$  years, respectively. Golden curves correspond to contribution to the basin density from axion-bremsstrahlung, and the red curves correspond to contribution from axion-Compton scattering. The figure and its description is taken from [9].

For our computations in the upcoming chapters, we use the local axion energy density in the fiducial limit produced from axion-bremsstrahlung and axion-Compton processes, i.e., the solid black curve plotted in fig.(4.4).

# Chapter 5

## Axion Basinschein

This chapter and the following one focus on the original research done in this thesis. Simply speaking, we combine the primary ideas from the two previous chapters :

- Chapter 3: In the axion rest-frame, an axion decays into two photons, each with an energy equal to half the axion mass. When an electromagnetic wave is already present at this energy, the decay rate is enhanced [34].
- Chapter 4: Stars can emit massive particles into bound orbits. These particles can form a density profile called the stellar basin around the star. Axions produced in the sun via axion-bremsstrahlung and Compton processes form a solar axion basin around the sun. Energy densities of this basin exceed those of the relativistic unbound solar axion flux [9].

By combining these two ideas, we estimate whether the detection of an echo signal is possible from the solar axion basin. The sun emits electromagnetic waves/photons over a spectrum of energy. From eq. (3.3), we understand that a stimulated decay occurs when the electromagnetic wave "exciting" the axion is precisely half of its mass (in natural units). From fig. (4.4), we can see that the energy density of the solar axion basin is varied as a function of its mass. If we consider electromagnetic waves/photons from the sun from different parts of the spectrum, we can estimate the echo signal from axion basins of a varied mass range. By this, we mean that the entire basin has the same axion mass, but we scan over different mass basins. We review basins made of varied axion masses because, at some masses, we have a higher energy density from the axion basin. At other masses, the intensity of the stimulating light is higher. We do a reasonably exhaustive search over various combinations of these two parameters.

Furthermore, we extend this exact idea to estimate (up to a zeroth order) the echo signal from the potential axion basins of other astrophysical compact

objects such as White Dwarf (WD) and Neutron Stars (NS). In this case, the electromagnetic waves that stimulate the axions will be either the compact objects themselves or a potential accretion disk around them.

The following table summarizes all the scenarios considered in this and the next chapter.

Axion Source	Stimulating source	Stimulating Frequency	Detecting instrument	Section
Solar basin	Sun	Soft X-Ray (Quiet sun)	Chandra	5.1.1
	Sun	Soft X-Ray (Flared Sun)	Chandra	5.1.2
	Sun	Ultraviolet	Hubble	5.2.1
	Sun	Optical	Hubble	5.2.2
	Sun	Infrared	Hubble	5.2.3
	White dwarf	Soft X Ray	Chandra	5.1.2
Neutron star basin	Neutron Star	Soft X Ray	Chandra	5.1.3
O-star basin	O-Star	Soft X Ray	Chandra	5.3
Milky Way's dark matter halo	Sun	Optical	Hubble NUV (CCD)	6.1
Average cosmological + dwarf galaxy + Milky Way's dark matter density	Radio galaxy	Radio	FAST	6.2

Table 5.1: Summary of all basinschein and haloschein scenarios estimated in chapter 5 and 6.

We perform calculations in the CGS unit system. Each computation's final results are presented in CGS and SI units. The numerical estimates, integrals, and generation of plots have been performed in Mathematica. While computing results in Mathematica, proper care has been taken to ensure correct units are being used.

Throughout this chapter and the following one, the axion-photon coupling is assumed to be the highest limit given in [44],

$$g_{a\gamma\gamma} = 6.6 \times 10^{-11} \text{ GeV}^{-1} \quad (5.1)$$

## 5.1 keV Axion Basinschein

### 5.1.1 keV solar axion basin

We compute the basinschein intensity from the solar axion basin by using the X-Ray spectra of the sun as our stimulating source. We assume a solar axion basin as discussed in section (4.3). From fig (4.4), the axion basin density can be read to be maximized when the axion mass corresponds to 3 keV (in the fiducial limit). This corresponds to a local axion density of  $\rho_0 = 10^{-4} \text{ GeV/cm}^3$  at 1 AU. We compute two quantities - echo signal (gegenschein) and signal that comes towards us directly from the sun (forwardschein). Using our central formula for such calculations eq.(3.4),

$$S_f = \frac{\hbar c^4}{16} (g_{a\gamma\gamma})^2 S_\nu (\nu_d) \underbrace{\int_{R_*}^{1 \text{ AU}} dx \rho_a [r(x)]}_{8.836 \times 10^{-9} \text{ g/cm}^2}, \quad (5.2)$$

$$S_g = \frac{\hbar c^4}{16} (g_{\alpha\gamma\gamma})^2 S_\nu (\nu_d) \underbrace{\int_{1 \text{ AU}}^{\infty} dx \rho_a [r(x)]}_{8.889 \times 10^{-16} \text{ g/cm}^2}. \quad (5.3)$$

where we have numerically integrated the column width corresponding to the number in the brace. The integrand is given by  $\rho_a[r(x)] = \rho_0 r^{-4}$ . The difference between the two formulas is the integration bounds. The bounds have been changed to represent the appropriate axion column. We will denote this integral by  $\rho_{\text{int}}$  and call it *integrated axion density*. For forwardschein, we take the integral over the axion basin density from the sun's surface to the Earth's surface. For the gegenschein signal, we use a column of solar axion from a Basin-Earth-Sun sequence. We let this integral go out to infinity, as the  $r^{-4}$  dependence of the density will ensure it converges fairly before infinity. This integration takes care of the fact that axion densities in these respective columns are significantly varied.

We now estimate numerical values for the forwardschein  $S_f$ , and gegenschein  $S_g$  signal, by plugging in the appropriate values for the specific intensity  $S_\nu (\nu_d)$  responsible for the stimulated decay. We will use maximized values to overestimate our signal, i.e., to get an upper bound estimate from our calculations. For a basin consisting of axions of  $m_a = 3 \text{ keV}$ , the stimulating frequency is given by,

$$\nu(m_a = 3 \text{ keV}) = \frac{m_a c^2}{2h} \quad (5.4)$$

$$= 3.628 \times 10^{17} \text{ Hz} \quad (5.5)$$

$$\lambda(m_a = 3 \text{ keV}) = 0.826 \text{ nm} \quad (5.6)$$

In this case, the energy of our stimulating corresponds to  $E_\gamma \approx 1.5 \text{ keV}$ . This is the same energy we expect for the basinschein photons we want to detect.

For the keV basin, we consider two cases for the corresponding X-ray sources from our sun.

### 5.1.1.1 Case I : Quiet Sun

At this wavelength, we have  $S = 1 \times 10^{-8} \text{ W m}^{-2}$  in the range  $\lambda \in [0.1, 0.8] \text{ nm}$  [45]. Assuming that solar flux at  $\lambda(m_a = 3 \text{ keV}) = 0.826 \text{ nm}$  is approximately similar to  $S(\lambda = 0.8 \text{ nm})$ , we have

$$S_\nu (\lambda = 0.8 \text{ nm}) = S_\nu (\nu = 3.63 \times 10^{17} \text{ Hz}) = 3.81 \times 10^{-24} \text{ g s}^{-2} \quad (5.7)$$

$$= 0.381 \text{ Jy} \quad (5.8)$$

$$= 3.81 \times 10^{-27} \text{ W m}^{-2} \text{ Hz}^{-1} \quad (5.9)$$

$$(5.10)$$

Using the above value for our solar flux in eq.(5.2) and (5.3), we get the

following values for forwardschein and gegenschein flux,

$$S_f = 3.04 \times 10^{-36} \text{ W m}^{-2}, \quad (5.11)$$

$$S_g = 3.06 \times 10^{-43} \text{ W m}^{-2}. \quad (5.12)$$

### 5.1.1.2 Case II : Solar Flares

We now consider the stimulating flux from the sun during solar flares. We used an extreme solar flare event, as shown in fig.(5.1). Other extreme solar flare events can be found in [46]. Focusing on the top panel of this figure, we can deduce that approximately between 0730 and 8000 hours UTC, there is an X-flare event for several minutes, corresponding to,

$$S = 2 \times 10^{-3} \text{ W m}^{-2}. \quad (5.13)$$

Although, later, when we assume the timescale of such a flare, we assume it to last for several hours, which will be an overestimate. Even in such an extreme overestimate, we will see that the number of forwardschein photons we expect to receive is significantly low.

Assuming a constant contribution from this flux in the bin corresponding to  $\nu \in [0.1, 0.8] \text{ nm}$ , we get

$$S_\nu(\lambda = 0.8 \text{ nm}) = 7.624 \times 10^{-19} \text{ g s}^{-2} \quad (5.14)$$

$$= 76240 \text{ Jy} \quad (5.15)$$

$$= 7.624 \times 10^{-22} \text{ W m}^{-2} \text{ Hz}^{-1}. \quad (5.16)$$

We estimate the forwardschein and gegenschein flux from the 3 keV solar axion basin,

$$S_f = 6.09 \times 10^{-31} \text{ W m}^{-2}, \quad (5.17)$$

$$S_g = 6.12 \times 10^{-38} \text{ W m}^{-2} \quad (5.18)$$

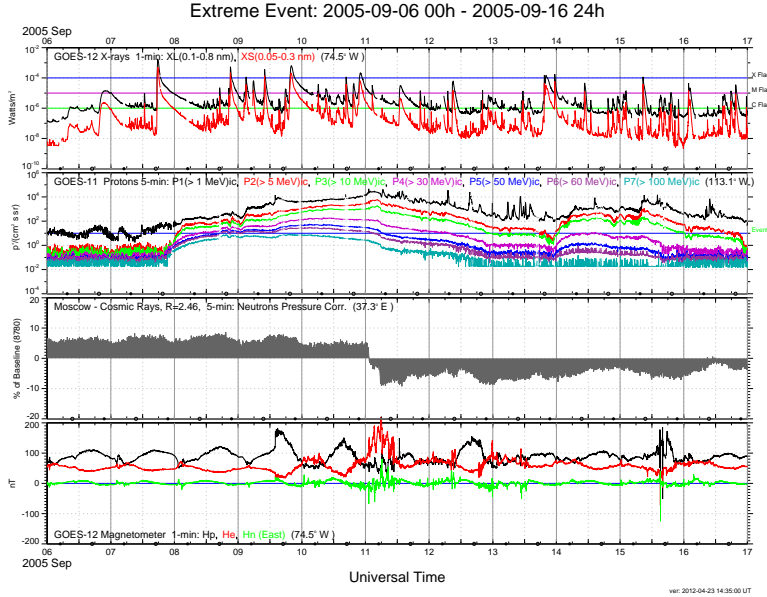


Figure 5.1: An extreme solar flare X-ray event in frequency  $\nu \in [0.1, 0.8]$  nm recorded on 6 Sept 2005. The figure is taken from [46].

### 5.1.2 Axion forwardschein from a white dwarf basin

As mentioned in the introduction to this chapter, we extend our idea for basinschein to other stellar compact objects. This section computes a forwardschein flux from a white dwarf axion basin. As a zeroth order estimate, we assume the axion basin is similar to the sun, i.e., it has the same energy density at 1 AU as in the fig.(4.4). Similar to sec. 5.1.1, we consider a basin consisting of 3 keV axions. The axion density profile is similar to the sun, yet we will significantly boost the integrated axion density as the white dwarf has a substantially smaller radius than the sun. Our axion density scales as the radius to the negative power of four; this gives us a tremendous boost as the integral  $\rho_{\text{int}}$  bound goes up to the surface of the white dwarf. Unfortunately, we will see that the stimulating flux  $S_\nu(\lambda = 0.8 \text{ nm})$  is much weaker than the sun.

Using our central formula eq.(3.4),

$$S_{f\text{WD}} = \frac{\hbar c^4}{16} (g_{a\gamma\gamma})^2 S_{\nu\text{WD}}(\nu_d) \underbrace{\int_{R_{\text{WD}}}^{\infty} dx \rho_a[r(x)]}_{\rho_{\text{int}}=0.173 \text{ g/cm}^2} \quad (5.19)$$

The upper bound of this integral goes till infinity, as the contribution from  $\rho_a[r(x)] \sim r^{-4}$  will nullify rapidly after a certain point, and barely contribute to  $\rho_{\text{int}}$ . As expected, the  $\rho_{\text{int}}$  quoted in eq. (5.19) orders of magnitude greater than the sun.

To get a strong source that will stimulate the decay, we consider a basin of a WD X-ray binary like KPD 0005+5106, which is active in the X-ray spectrum. The radius of the WD is  $R_{\text{WD}} = 0.006 R_{\odot}$  and its distance to Earth is 1300 ly [47, 48]. The flux in the range  $E_{\gamma} \in [0.6, 3] \text{ keV}$  is,

$$S = 2.05 \times 10^{-16} \text{ W m}^{-2}. \quad (5.20)$$

Assuming a constant flux throughout the range, we get the flux density as,

$$S_{\nu \text{WD}}(\lambda = 0.8 \text{ nm}) = 5.63 \times 10^{-32} \text{ g s}^{-2} \quad (5.21)$$

$$= 5.63 \times 10^{-9} \text{ Jy} \quad (5.22)$$

$$= 5.63 \times 10^{-35} \text{ W m}^{-2} \text{ Hz}^{-1} \quad (5.23)$$

Plugging this in Eq.(5.19), we get the forwardschein irradiance as

$$S_{f \text{WD}} = 8.78 \times 10^{-38} \text{ W m}^{-2} \quad (5.24)$$

### 5.1.3 Axion forwardschein from a neutron star axion basin

In this section, we perform an estimation similar to the previous section on a neutron star instead of a white dwarf. The radius of a neutron star is at least a few orders smaller than a white dwarf, giving us an even stronger contribution to the integrated column density. The energy density of the axion basin is again assumed similar to the sun to a zeroth order. We take the radius of the neutron star to be  $R_{\text{NS}} = 10 \text{ km}$ .

$$S_{f \text{NS}} = \frac{\hbar c^4}{16} (g_{a\gamma\gamma})^2 S_{\nu \text{NS}}(\nu_d) \underbrace{\int_{R_{\text{NS}}}^{\infty} dx \rho_a[r(x)]}_{\rho_{\text{int}} = 2.98 \times 10^6 \text{ g/cm}^2} \quad (5.25)$$

By taking a typical radius of a neutron star, we see  $\rho_{\text{int}}$  got a tremendous boost compared to our previous scenarios. Unfortunately, as we will see below, the  $S_{\nu \text{NS}}(\nu_d)$  is especially poor, which effectively cancels out this boost. Neutron stars are weak at producing photons. Furthermore, most are orders of magnitude further away from Earth than the sun.

For  $S_{\nu \text{NS}}$  we use the flux density from X-ray binary GX 17+2 [49]. It estimates that the BeppoSAX telescope captures approximately one photon per centimeter squared, per second, per keV from GX 17+2. While computing prospective forwardschein photon numbers in section 5.1.4, we assume that we are getting the same count as in [49], but for Chandra X-ray observatory, which has a better effective area than BeppoSAX telescope. We convert this photon count to a specific intensity,

$$S_{\nu \text{NS}} = (1 \text{ photon cm}^{-2} \text{ s}^{-1} \text{ keV}^{-1}) \times \hbar \times 3 \text{ keV} \quad (5.26)$$

$$= 1.58 \times 10^{-28} \text{ g s}^{-2} \quad (5.27)$$

$$= 1.58 \times 10^{-6} \text{ Jy} \quad (5.28)$$

$$= 1.58 \times 10^{-31} \text{ W m}^{-2} \text{ Hz}^{-1} \quad (5.29)$$

$$(5.30)$$

Plugging this in eq.(5.19), we get the forwardschein flux as

$$S_{f\text{NS}} = 4.25 \times 10^{-26} \text{ W m}^{-2} \quad (5.31)$$

### 5.1.4 Projected photon numbers

We use the Chandra X-ray observatory to estimate the photon numbers from the above measurements. Compared to radio or optical wavelength astronomy, where it primarily makes sense to talk about the flux of the received signal, the X-ray domain talks about photon numbers from the received signal. An integer number of X-ray photons detected over reasonable exposure time suffices as a measurable signal [50].

The effective area for the mirror on Chandra is  $A_{\text{eff}} = 800 \text{ cm}^2$  in 0.5-2 keV energy range [51]. This is our range of interest as  $\lambda \in [0.1, 0.8] \text{ nm}$  corresponds to photon energies in  $E_\gamma \in [1.5, 13] \text{ keV}$ . We see that even with an optimistic constant area of  $800 \text{ cm}^2$ , we get a poor photon number for all the cases that we covered in sections 5.1.1, 5.1.2, and 5.1.3.

The results are summarised in the following table :

<i>Axion Source</i>	<i>Photon energy (keV)</i>	<i>Total photons <math>N_{\gamma\text{tot}}</math></i>	<i>Forwardschein photons <math>N_{\gamma\text{FS}}</math></i>	<i>Gegenschein photons <math>N_{\gamma\text{GS}}</math></i>
Quiet Sun (5.1.1.1)	1.5	$1.39 \times 10^9$	$3.65 \times 10^{-16}$	$3.67 \times 10^{-23}$
Solar Flares (5.1.1.2)	1.5	$2.78 \times 10^{13}$	$6.57 \times 10^{-11}$	$7.34 \times 10^{-19}$
White Dwarf (5.1.2)	1.5	16.39	$8.41 \times 10^{-18}$	NA
Neutron Star (5.1.3)	1.5	57600	$5.1 \times 10^{-6}$	NA

Table 5.2: Summary of keV basinschein photons estimated by Chandra X-ray observatory from axion basins of the sun, a white dwarf and a neutron star.

where the following formulas are used to compute the photon numbers,

$$N_{\gamma\text{tot}} = \frac{S_\nu \times T_{\text{obs}} \times A_{\text{eff}}}{E_\gamma} \times (\text{binwidth}) \quad (5.32)$$

$$N_{\gamma\text{FS}} = \frac{S_f \times T_{\text{obs}} \times A_{\text{eff}}}{E_\gamma} \quad (5.33)$$

$$N_{\gamma\text{GS}} = \frac{S_g \times T_{\text{obs}} \times A_{\text{eff}}}{E_\gamma}. \quad (5.34)$$

The *binwidth* factor in  $N_{\gamma\text{tot}}$  comes because we are measuring signal from a continuum. In contrast, for forwardschein or gegenschein, we look for a signal peaked around a particular frequency (Also, a good check for the necessity of that factor is by realizing that  $S_\nu$  and  $S_f$  differ in units by a factor of Hz). The

exposure time  $T_{\text{obs}}$  is taken to be 100 h, except for the case of solar flares where we take  $T_{\text{obs}} = 10$  h as an overestimate.

## Conclusion

We can see from table.(5.2) that none of the forwardschein or gegenschein photon numbers are anywhere close to an integer number, which, as we discussed earlier, corresponds to a measurable signal. The closest we get to an integer number is in the case of a forwardschein from a neutron star basin. In the future, if any rigorous neutron star basin calculation estimates to have an exceptionally high axion basin density than what we considered here, we could potentially get a measurable signal.

## 5.2 Solar Axion Basinschein

This section calculates the prospective forwardschein signal from the solar axion basin analogous to section 5.1.1. The difference is that we look at other possible masses instead of assuming 3 keV axions in the basin. Different mass scales mean we need solar flux at different wavelengths to stimulate axion decay. For a given axion mass, we know the corresponding frequency of photon required to facilitate the decay by eq.(3.3). The axion density needed for the basin at those corresponding masses can be extracted from fig.(4.4).

To compute the gegenschein/forwardschein from the solar basin, we need the specific intensity of our sun at various wavelengths. These values can be extracted from the following plot,

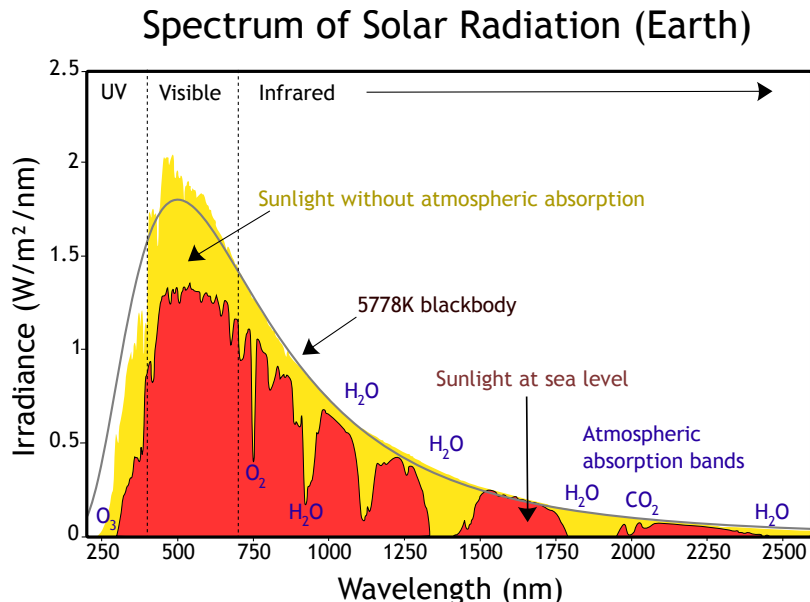


Figure 5.2: Spectrum of solar radiation. The figure is taken from [52].

### 5.2.1 Solar basinschein : Ultraviolet (UV)

We start by looking at the UV range of the sun. Assuming the axion density to be stimulated by photons of wavelength  $\lambda_{\text{UV}} = 325 \text{ nm}$ , the axions should be made up of mass  $m_a^{\text{UV}} = 7.63 \text{ eV}$  using eq.(3.3). From the fig.(4.4), we can see that this corresponds to a local axion density of  $\rho_a = 5 \times 10^{-10} \text{ GeV cm}^{-3}$ . From fig.(5.2), we can see that,

$$S_\lambda(\lambda_{\text{UV}}) = 0.75 \text{ W m}^{-2} \text{ nm}^{-1} \quad (5.35)$$

We convert this into units per frequency instead of per wavelength using the following formula

$$\frac{S_\nu}{S_\lambda} = \frac{\lambda^2}{c} \quad (5.36)$$

Rearranging and plugging in the appropriate values,

$$S_\nu(\lambda_{\text{UV}}) = \frac{(325 \text{ nm})^2}{c} S_\lambda \quad (5.37)$$

$$= 2.64 \times 10^{-13} \text{ W m}^{-2} \text{ Hz}^{-1} \quad (5.38)$$

$$= 2.64 \times 10^{13} \text{ Jy} \quad (5.39)$$

Using our central formula for these calculations eq.(3.4), we get,

$$S_f(\lambda_{\text{UV}}) = \frac{\hbar c^4}{16} (g_{a\gamma\gamma})^2 S_\nu(\lambda_{\text{UV}}) \underbrace{\int_{R_*}^{1 \text{ AU}} dx \rho_a[r(x)]}_{4.41 \times 10^{-14} \text{ g/cm}^2} \quad (5.40)$$

$$= 1.05 \times 10^{-27} \text{ W m}^{-2} \quad (5.41)$$

$$S_g(\lambda_{\text{UV}}) = \frac{\hbar c^4}{16} (g_{a\gamma\gamma})^2 S_\nu(\lambda_{\text{UV}}) \underbrace{\int_{1 \text{ AU}}^{\infty} dx \rho_a[r(x)]}_{4.44 \times 10^{-21} \text{ g/cm}^2} \quad (5.42)$$

$$= 1.06 \times 10^{-34} \text{ W m}^{-2} \quad (5.43)$$

**Flux ratio** We want to compute the flux ratio  $\Phi_R$  for our forwardschein signal versus the regular UV signal from the sun at  $\lambda_{\text{UV}}$ . For the regular flux received from the sun, we need to know the spectral resolution of our telescope. In this scenario, we use the Near UltraViolet channel (NUV) of the Cosmic Origins Spectrograph (COS) on HST. It has a spectral resolving power ( $R = \lambda/\Delta\lambda$ ) of  $R_{\text{NUV}} = 2000$  [53] giving us,

$$\text{binwidth}_{\text{NUV}}(\lambda_{\text{UV}}) = \frac{m_a(\lambda_{\text{UV}})}{2\hbar} \frac{1}{R_{\text{NUV}}} = 2.90 \times 10^{12} \text{ s}^{-1} \quad (5.44)$$

$$\Phi_R(\lambda_{\text{UV}}) = \frac{S_f(\lambda_{\text{UV}})}{S_\nu(\lambda_{\text{UV}}) \times \text{binwidth}_{\text{NUV}}(\lambda_{\text{UV}})} = 1.38 \times 10^{-26} \quad (5.45)$$

### 5.2.2 Solar basinschein : Optical (OP)

The sun is most active in the optical range. Here, we assume the axion density to be stimulated by photons of wavelength  $\lambda_{\text{OP}} = 500 \text{ nm}$ . Hence, the corresponding axion density needs to be assumed to be made of axions of mass  $m_{a\text{OP}} = 4.96 \text{ eV}$  using eq.(3.3). From fig.(4.4), we extrapolate that this corresponds to a local axion density of  $\rho_a = 7.5 \times 10^{-11} \text{ GeV cm}^{-3}$ . From fig. (5.2),

$$S_\lambda(\lambda_{\text{OP}}) = 1.75 \text{ W m}^{-2} \text{ nm}^{-1} \quad (5.46)$$

Converting  $S_\lambda$  to  $S_\nu$ ,

$$S_\nu(\lambda_{\text{OP}}) = \frac{(500 \text{ nm})^2}{c} S_\lambda \quad (5.47)$$

$$= 1.46 \times 10^{-12} \text{ W m}^{-2} \text{ Hz}^{-1} \quad (5.48)$$

$$= 1.45 \times 10^{14} \text{ Jy} \quad (5.49)$$

Using our central formula for these calculations eq.(3.4), we get,

$$S_f(\lambda_{\text{OP}}) = \frac{\hbar c^4}{16} (g_{a\gamma\gamma})^2 S_\nu(\lambda_{\text{OP}}) \underbrace{\int_{R_*}^{1 \text{ AU}} dx \rho_a[r(x)]}_{6.63 \times 10^{-15} \text{ g/cm}^2} \quad (5.50)$$

$$= 8.74 \times 10^{-28} \text{ W m}^{-2} \quad (5.51)$$

$$S_g(\lambda_{\text{OP}}) = \frac{\hbar c^4}{16} (g_{a\gamma\gamma})^2 S_\nu(\lambda_{\text{OP}}) \underbrace{\int_{1 \text{ AU}}^{\infty} dx \rho_a[r(x)]}_{6.67 \times 10^{-22} \text{ g/cm}^2} \quad (5.52)$$

$$= 8.79 \times 10^{-35} \text{ W m}^{-2} \quad (5.53)$$

**Flux-ratio** We compute the flux ratio for our forwardschein signal versus the regular optical signal from the sun at  $\lambda_{\text{OP}}$ . For the regular flux received from the sun, we need to know the spectral resolution of our telescope detector. In this scenario, we use the CCD first-order spectroscopy grating G430L of the STIS on HST. It has a spectral resolving power of  $R_{\text{G430L}} \approx 1000$  [53], giving us,

$$\text{binwidth}_{\text{NUV}}(\lambda_{\text{OP}}) = \frac{m_a(\lambda_{\text{OP}})}{2\hbar} \frac{1}{R_{\text{G430L}}} = 3.77 \times 10^{12} \text{ s}^{-1} \quad (5.54)$$

$$\Phi_R(\lambda_{\text{OP}}) = \frac{S_f(\lambda_{\text{OP}})}{S_\nu(\lambda_{\text{OP}}) \times \text{binwidth}_{\text{NUV}}(\lambda_{\text{OP}})} = 1.59 \times 10^{-28} \quad (5.55)$$

### 5.2.3 Solar basinschein : Infrared (IR)

Finally, we consider the infrared range of the sun as the stimulating source. Assuming that we want the axion density to be stimulated by photons of wavelength  $\lambda_{\text{IR}} = 1500 \text{ nm}$ , the axion density would be made up of mass  $m_{a\text{UV}} = 1.65 \text{ eV}$  using eq.(3.3). From fig.(4.4), we extrapolate that this corre-

sponds to a local axion density of  $\rho_a = 7.5 \times 10^{-11} \text{ GeV cm}^{-3}$ .

From fig.(5.2) we read,

$$S_\lambda(\lambda_{\text{IR}}) = 0.3 \text{ W m}^{-2} \text{ nm}^{-1} \quad (5.56)$$

Converting  $S_\lambda$  to  $S_\nu$ ,

$$S_\nu(\lambda_{\text{IR}}) = \frac{(1500 \text{ nm})^2}{c} S_\lambda \quad (5.57)$$

$$= 2.25 \times 10^{-12} \text{ W m}^{-2} \text{ Hz}^{-1} \quad (5.58)$$

$$= 2.25 \times 10^{14} \text{ Jy} \quad (5.59)$$

We use our central formula for the forwardschein, which gives us,

$$S_f(\lambda_{\text{IR}}) = \frac{\hbar c^4}{16} (g_{a\gamma\gamma})^2 S_\nu(\lambda_{\text{IR}}) \underbrace{\int_{R_*}^{1 \text{ AU}} dx \rho_a[r(x)]}_{2.65 \times 10^{-16} \text{ g cm}^{-2}} \quad (5.60)$$

$$= 1.05 \times 10^{-27} \text{ W m}^{-2} \quad (5.61)$$

$$S_g(\lambda_{\text{IR}}) = \frac{\hbar c^4}{16} (g_{a\gamma\gamma})^2 S_\nu(\lambda_{\text{IR}}) \underbrace{\int_{1 \text{ AU}}^{\infty} dx \rho_a[r(x)]}_{2.66 \times 10^{-23} \text{ g/cm}^2} \quad (5.62)$$

$$= 5.42 \times 10^{-36} \text{ W m}^{-2} \quad (5.63)$$

**Flux-ratio** We want to compute the flux ratio  $\Phi_R$  for our forwardschein signal versus the regular optical signal from the sun at  $\lambda_{\text{IR}}$ . For the regular flux received from the sun, we need to know the spectral resolution of our telescope detector. In this scenario, we use the CCD first-order spectroscopy grating G750L of the STIS on HST. It has a spectral resolving power of  $R_{\text{G750L}} \approx 1000$  [53], giving us,

$$\text{binwidth}_{\text{NUV}}(\lambda_{\text{IR}}) = \frac{m_a(\lambda_{\text{IR}})}{2\hbar} \frac{1}{R_{\text{G750L}}} = 1.25 \times 10^{12} \text{ s}^{-1} \quad (5.64)$$

$$\Phi_R(\lambda_{\text{IR}}) = \frac{S_f(\lambda_{\text{IR}})}{S_\nu(\lambda_{\text{IR}}) \times \text{binwidth}_{\text{NUV}}(\lambda_{\text{IR}})} = 1.91 \times 10^{-29} \quad (5.65)$$

## Conclusion

All of the forwardschein and gegenschein estimates  $S_{f,g}(\lambda_{\text{UV}}, \lambda_{\text{OP}}, \lambda_{\text{OP}})$  and the flux ratios  $\Phi_R(\lambda_{\text{UV}}, \lambda_{\text{OP}}, \lambda_{\text{OP}})$  are orders of magnitude away from measurable signals. There is no possibility of detection of basinschein signals from all the scenarios considered in the chapter above.

## 5.3 O-star forwardschein estimate

The basinschein flux depends upon the flux density. We assume a basin density like fig.(4.4) around a hypothetical O-star, which has a higher flux density than

our sun.

Using Planck's radiation law,

$$S_\lambda(\lambda, T) = \frac{2\pi hc^2}{\lambda^5 e^{\frac{hc}{\lambda k_B T}} - 1} \quad (5.66)$$

we can compare the blackbody spectrum of an O-star with a temperature of 50000 K with our sun, which has a surface temperature of  $T = 6000$  K.

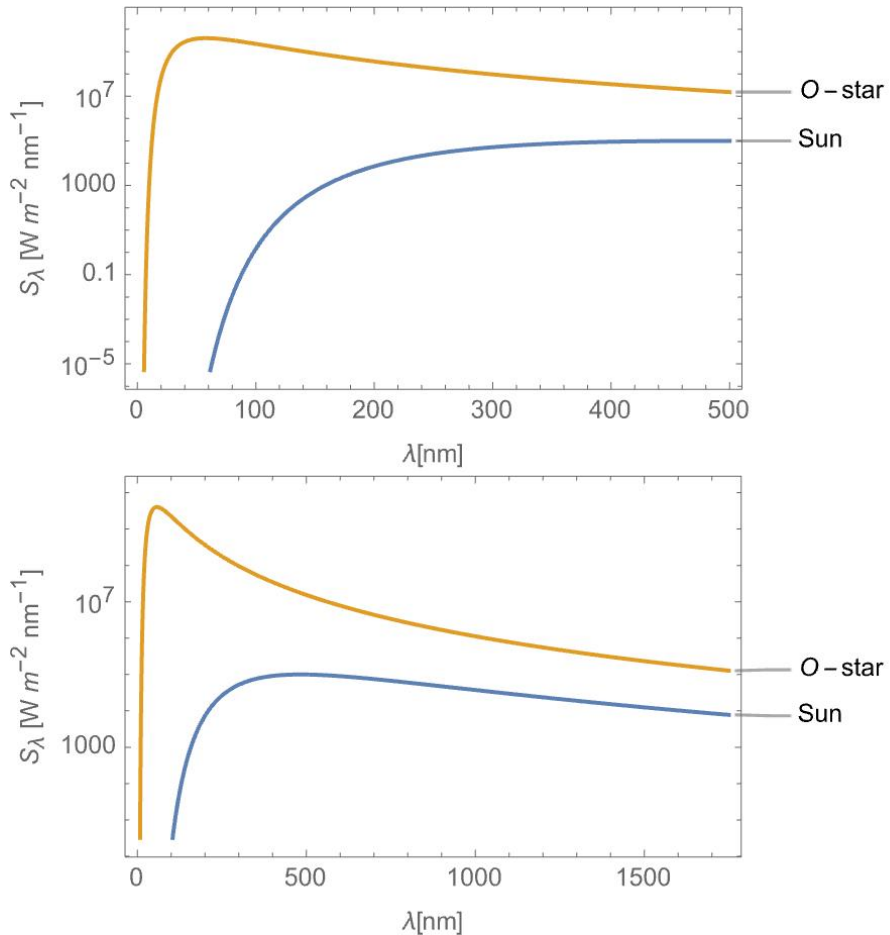


Figure 5.3: *Top:* Flux density of sun versus an O-star ( $T = 50000$  K) in the wavelength  $\lambda \in [0, 500]\text{nm}$ . *Bottom:* Flux density of sun versus an O-star in the wavelength  $\lambda \in [0, 1500]\text{nm}$

## Conclusion

We can see that we get a few orders of magnitude boost in  $S_\nu$  across all the wavelengths we considered in the previous sections. This boost, unfortunately, does not overcome the fact that we still end up with a meager flux ratio. It would

be as large as a few orders of magnitude in comparison to eq.(5.45), (5.55), (5.65), which is still extremely low to be detected.

# Chapter 6

## Axion Haloschein

This chapter computes the axion echo from the Milky Way's dark matter halo. We assume that the entire halo is made out of axions.

We preserve the units on numerical values borrowed from sources. We perform calculations in the CGS unit system. Each computation's final results are presented in CGS and SI units. The numerical estimates, integrals, and generation of plots have been performed in Mathematica. While computing results in Mathematica, proper care has been taken to ensure correct units are being used.

As discussed earlier, we need our dark matter halo's density profile to compute the axion echo signal. We use a standard Milky Way's Navarro-Frenk-White (NFW) profile halo [13], given by the following equation,

$$\rho_{\text{MW}}(r) = \frac{\rho_0}{(r/r_s)(1+r/r_s)^2}, \quad (6.1)$$

where  $r$  is the galactocentric radius and  $r_s = 16$  kpc the scale radius.

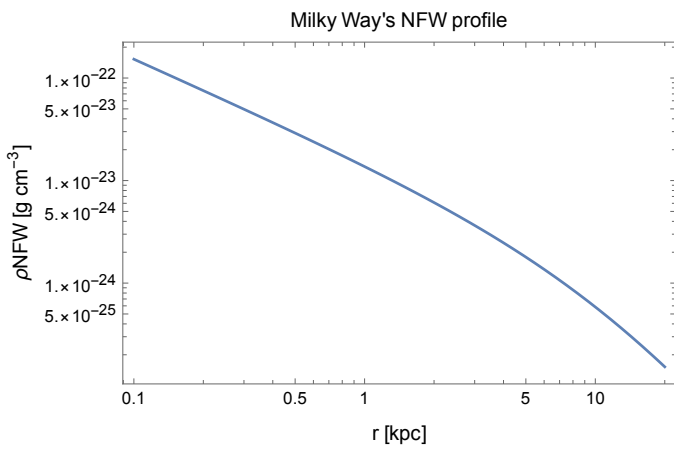


Figure 6.1: Milky Way's DM halo density modeled using the NFW profile

The local density  $\rho_0$  at the solar position  $r_\odot = 8.22$  kpc is  $\rho(r_\odot) = 0.46 \text{ GeV cm}^{-3}$ .

In fig.(6.1) we plot eq.(6.1) as a function of the galactocentric radius.

Next, we compute the integrated DM column density, i.e.,  $\rho_{\text{int}}$ . To do this, we define a few variables, such as

$$r_{\text{col}}(x, \theta) = \sqrt{\tilde{x}^2 + r_{\odot}^2 - 2\tilde{x}r_{\odot} \cos \theta_s}, \quad (6.2)$$

where  $\tilde{x}, r, \theta_s, r_{\odot}$  are defined in fig.(6.2).

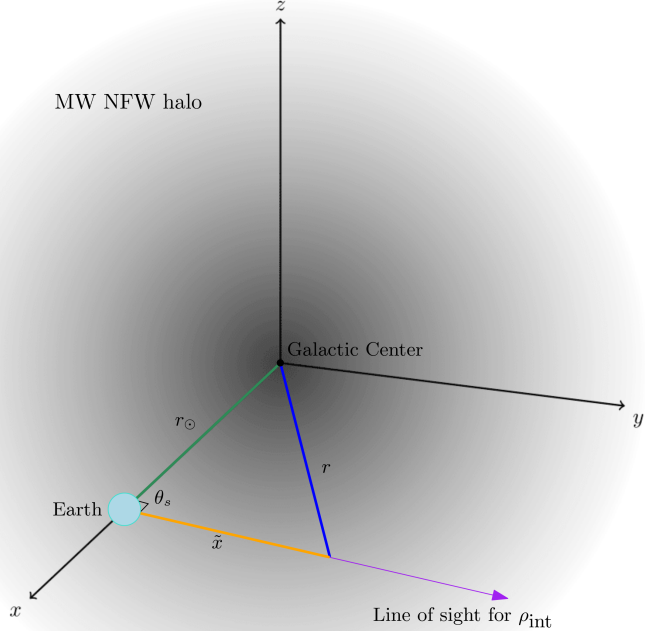


Figure 6.2: Schematic for gegenschein geometry from the Milky Way's DM halo. The figure is inspired from [34]

By plugging  $r_{\text{col}}$  into  $\rho_{\text{MW}}$ , we compute the DM density of the NFW halo along line of sight from our perspective. The line of sight will be defined by an angle  $\theta_s$ . After choosing a  $\theta_s$ , we then integrate over  $\tilde{x}$  to get the DM integrated column density along that line of sight. As shown in the figure, we choose our integral at an angle of  $\theta_s = \pi/2$ . We can then perform an integral over  $\tilde{x}$  from 0 to  $\infty$  (As we can see in fig.(6.1), most of our DM density comes from the first few kilo-parsecs, and then it decreases rapidly). Integrating numerically estimates the integrated axion density in this scenario to be,

$$\rho_{\text{int}} = \int_{\tilde{x}=0}^{\tilde{x}=\infty} \rho \left( r_{\text{col}} \left( \tilde{x}, \frac{\pi}{2} \right) \right) d\tilde{x} = 0.0323 \text{ g cm}^{-2}. \quad (6.3)$$

This integrated axion density is overestimated as the DM halo will have a

transverse velocity dispersion that will smear out the gegenschein signal. Other effects like doppler broadening will also weaken our signal (we did integrate  $\tilde{x}$  up to infinity, which to some extent also contributes to the overestimate). A more general geometry of gegenschein calculation by considering the effects mentioned above is explained brilliantly in section II.B of [13]. We work with our overestimated value of the  $\rho_{\text{int}}$  as a zeroth order estimate. As we will see, even in this exaggerated scenario, the gegenschein signal is extremely low.

## 6.1 Axion Haloschein from the solar optical band

We compute axion gegenschein from the Milky Way's dark matter halo in the range where the sun provides us with the highest electromagnetic flux, i.e., at  $\lambda = 500$  nm. The assumed mass of the axions in the halo is computed by eq.(3.3) which gives us  $m_a = 4.95$  eV. We know that mass is slightly above the current bounds on DM axions. Nevertheless, the computation was performed to get an order of magnitude estimate on the gegenschein signal. In the case of an optimistic gegenschein signal, we would have moved to a halo made out of lower mass axions. This won't be necessary as we already mentioned that we find a feeble gegenschein signal.

We compute the gegenschein signal using eq.(3.4),

$$S_g = \frac{\hbar c^4}{16} (g_{a\gamma\gamma})^2 S_\nu (\nu_d) \underbrace{\int dx \rho_a [r(x)]}_{\rho_{\text{int}}=0.0323 \text{ g/cm}^2} \quad (6.4)$$

$$= 4.23 \times 10^{-12} \text{ g s}^{-3} \quad (6.5)$$

$$= 4.23 \times 10^{-15} \text{ W m}^{-2}, \quad (6.6)$$

where  $\rho_{\text{int}}$  is taken from eq.(6.3). We used  $S_\nu (\lambda = 500 \text{ nm}) = 1.45 \times 10^{14} \text{ Jy}$  from eq.(5.49).

### Signal to Noise Ratio (SNR)

We compute the gegenschein signal's SNR using Hubble Space Telescope's (HST) Space Telescope Imaging Spectrograph (STIS). First, we calculate the SNR analytically. Ignoring all background noise to get an upper bound for the signal, we have our SNR formula [54],

$$\text{SNR} = \frac{S_c}{N} = \frac{S_c}{\sqrt{S_c + N_{\text{pix}} \text{DC}_c}}, \quad (6.7)$$

where  $S_c$  is the source counts,  $N_{\text{pix}}$  is the number of pixels used for detection and  $\text{DC}_c$  is the Dark Current count. A good explanation of dark currents and their role in CCD detection is explained in appendix E. In the same appendix, we explain why  $\text{DC}_c$  can't be nullified while estimating an upper bound for SNR (unlike the background noise, which is assumed to be null while computing the

upper bound). We take DC = 0.029 per pixel per second [55]. This gives us  $\text{DC}_c = \text{DC} \cdot t_e$  where  $t_e$  is the exposure time. We need  $S_c$  to calculate the SNR. We estimate the source count using the following formula,

$$S_c = \frac{S_g \times t_e \times A_{\text{eff}}}{h(c/\lambda)} \times \underbrace{\frac{1}{4\pi} \times \left( \frac{\theta_{\text{aperture}}}{N_{\text{pix}}} \right)^2}_{\text{Geometrical factor}}, \quad (6.8)$$

where,

- $S_c$  is the photon counts per pixel
- $S_g$  is the flux of gegenschein signal
- $t_e$  is the exposure time
- $A_{\text{eff}}$  is the effective collecting area
- $(\theta_{\text{aperture}})^2$  gives the field of view angle for our CCD detector (We get a deg<sup>2</sup> units for this term in the equation which cancels out with the sr<sup>-1</sup>)
- $(N_{\text{pix}})^2$  factor makes sure that we are computing the counts for per pixel in an array of  $N_{\text{pix}} \times N_{\text{pix}}$  pixels.

**Note:** In chapter 5, we did not use the geometrical factor for HST as we were trying to make upper bound estimates. We assumed the geometrical factor to be unity. This means we assumed that our detector could pick up the signal from 360° around it. Even after considering such an exaggerated detector, the upper bound estimates were y too low, and considering the geometrical factor would decrease it further. We consider it in this calculation because we had an incredibly optimistic SNR for this scenario. Unfortunately, we were blindsided because the noise from the dark current was not considered.

The 1/4 $\pi$  factor ensures that we are looking at a point source with units of sr<sup>-1</sup>. Finally, we divide by the energy of the photon  $h\nu$  to give us a photon count. For STIS, we have,

$$\theta_{\text{aperture}} = 0.51 \text{ arcsecs}, \quad N_{\text{pix}} = 1024, \quad A_{\text{eff}} = 4.5 \text{ m}^2 \quad (6.9)$$

Plugging all the numbers in, for an exposure time of 100 hours at  $\lambda = 500 \text{ nm}$  we get,

$$S_c = 8 \times 10^{-5} \text{ per pixel} \quad (6.10)$$

As  $S_c$  is in units per pixel, we take the  $N_{\text{pix}} = 1$  while computing the SNR. Plugging all the numbers in eq.(6.7),

$$\text{SNR} = 7.82 \times 10^{-7}. \quad (6.11)$$

The primary reason for such an extremely low SNR is the dark currents. Just for reference, our first calculation was done without the knowledge of dark currents in CCD,

$$\text{SNR}_{\text{woDC}} = \frac{S_c}{\sqrt{S_c}} = 8.94 \times 10^{-3}. \quad (6.12)$$

This is a highly optimistic number as HST has data for several years compared to the hundred hours of exposure time considered for the calculation. As a result, we computed the SNR with greater precision as we believed eq.(6.12) to be our upper bound.

We perform this calculation with the aid of Hubble Space Telescope's STIS exposure time calculator<sup>1</sup>. This tool calculates the count rates and SNR for a simulated spectrum of one source in a STIS spectroscopic observation. Simply, it computes the SNR for a given exposure time or calculates the required exposure time for the user-given SNR. The tool allows the user to provide a "User-Supplied Spectra"<sup>2</sup>. Following the instructions, we generated a Gaussian with  $\mu = 500$  nm and  $\sigma = 5$  as shown in fig.(6.3). This was used as input for the "User-Supplied Spectra." The calculator gave us an SNR estimate with the same order of magnitude to eq.(6.11) for an exposure time of 100 hours (The background noise factors were tuned down to be null, similar to the analytical case).

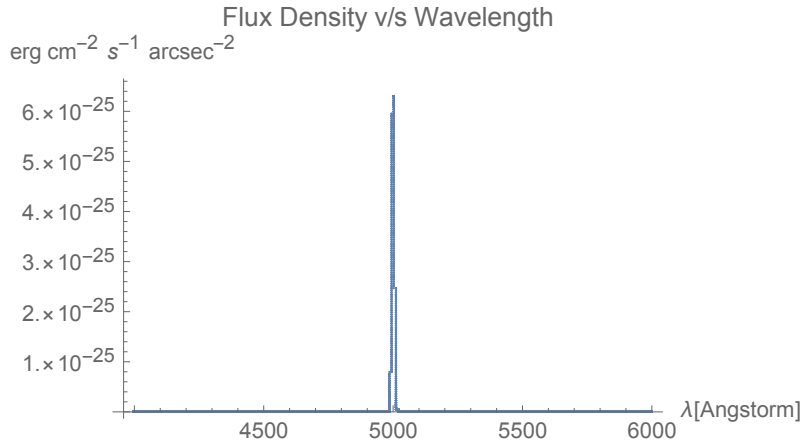


Figure 6.3: Gaussian wavepacket created in Mathematica to compute the SNR from Hubble's STIS exposure time calculator

## Conclusion

The SNR calculated for this scenario is extremely low. We do not expect any signature of gegenschein photons from the Milky Way's dark matter halo in the

---

<sup>1</sup><https://etc.stsci.edu/etc/input/stis/spectroscopic/>

<sup>2</sup>[https://etc.stsci.edu/etcstatic/users\\_guide/1\\_ref\\_5\\_user\\_spectra.html](https://etc.stsci.edu/etcstatic/users_guide/1_ref_5_user_spectra.html)

archived HST data in the optical regime.

## 6.2 Axion forwardschein from a distant radio galaxy source

In this section, we compute a forwardschein signal for a hypothetical scenario in which we have a radio galaxy at  $z = 1$  (we assume its spectrum similar to one of the brightest radio galaxies known to us, Cygnus A). The spectral flux density for Cygnus A is given by [34],

$$\log S_{A\nu_d}(\nu_d) = a + b \log \nu_d + c \log^2 \nu_d. \quad (6.13)$$

Here, we have  $a = 4.695$ ,  $b = 0.085$ ,  $c = -0.178$  when flux density  $S_{A\nu_d}$  is expressed in Jy and frequency in MHz. We plot this specific flux as a function of frequency,

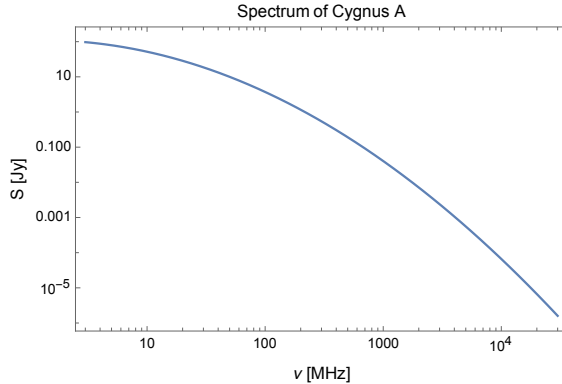


Figure 6.4: Spectral flux density of Cygnus A as a function of frequency

The electromagnetic signal from this radio galaxy travels through space from  $z = 1$  to  $z = 0$ , where it pierces through a dwarf galaxy at the edge of the Milky Way and then goes through the Milky Way's dark matter halo before it reaches Earth. All in all, the contribution to  $\rho_{\text{int}}$  in the forwardschein signal comes from three sources :

1.  $\rho_{\text{int}}(z = 1 \rightarrow 0)$ : Average dark density of an expanding flat FLRW universe from  $z = 1$  to  $z = 0$  (Section 6.2.1)
2.  $\rho_{\text{int}}(\text{LeoI})$ : Dark matter density from a dwarf galaxy at the edge of MW (Section 6.2.2)
3.  $\rho_{\text{int}}(\text{MW})$ : Dark matter density from the Milky Way's NFW dark matter halo (Eq.(6.3))

### 6.2.1 Cosmological integrated DM density

We want to compute the integrated DM column density from a (radio) galaxy approximately  $z = 1$  away from us. We start this calculation in a flat FLRW metric, with standard  $\Lambda$ CDM cosmology. We need two ingredients to compute  $\rho_{\text{int}}$ ,

$$\rho_{\text{int}} \equiv \int_{x(z=z_0)}^{x(z=0)} \rho(x) dx \quad (6.14)$$

$$= \int_{t(x(z=z_0))}^{t(x(z=0))} \rho(x) c dt \quad (6.15)$$

$$= c \int_{z=z_0}^{z=0} \rho(z) \frac{dt}{dz} dz. \quad (6.16)$$

The second equality comes from the chain rule after representing  $t$  in terms of  $z$ . Instead of integrating over proper distance, we can integrate over redshift for convenience. The two ingredients needed are,

1. The first ingredient needed is the average matter density in the universe as a function of redshift  $z$ , i.e.,  $\rho(z)$ . In terms of the scale factor  $a(t)$  we write,

$$\Omega_{m,0} = \frac{\rho_{m,0}}{\rho_{\text{crit}}}, \quad \rho_m = \rho_{m,0} \left( \frac{a_0}{a} \right)^3. \quad (6.17)$$

After setting  $a_0 = 1$  and substituting  $\rho_{m,0}$  from  $\Omega_{m,0}$  into  $\rho_m$  we get

$$\rho_m = \frac{\rho_{\text{crit}} \Omega_{m,0}}{a^3}. \quad (6.18)$$

We can now substitute  $a = (1+z)^{-1}$  to get,

$$\rho_m(z) = \rho_{\text{crit}} \Omega_{m,0} (1+z)^3. \quad (6.19)$$

2. The second ingredient needed to compute  $\rho_{\text{int}}$  is  $\frac{dt}{dz}$ , which can be computed as follows,

$$\frac{da}{dt} = aH, \quad (6.20)$$

which alternatively can be written as,

$$\frac{da}{dz} \frac{dz}{dt} = H \quad (6.21)$$

$$\frac{d}{dz} \left( \frac{1}{1+z} \right) \frac{dz}{dt} = \frac{H}{1+z} \quad (6.22)$$

$$\left( \frac{-1}{(1+z)^2} \right) \frac{dz}{dt} = \frac{H}{(1+z)} \quad (6.23)$$

$$\frac{dt}{dz} = \frac{-1}{H(1+z)}. \quad (6.24)$$

Plugging eq.(6.19), eq.(6.24) into eq.(6.16) we get,

$$\rho_{\text{int}}(z_0) = c \int_{z=z_0}^{z=0} \rho_{\text{crit}} \Omega_{m,0} (1+z)^3 \left( \frac{-1}{H(1+z)} \right) dz \quad (6.25)$$

$$= c \rho_{\text{crit}} \Omega_{m,0} \int_{z=0}^{z=z_0} \left( \frac{(1+z)^2}{H} \right) dz. \quad (6.26)$$

We use the following standard expression for the Hubble parameter in flat space [56],

$$H = H_0 \sqrt{\Omega_{m,0} (1+z)^3 + \Omega_{\Lambda,0} + \Omega_{r,0} (1+z)^4}. \quad (6.27)$$

We are primarily interested in signals coming from stars, and the first stars were born around  $z \simeq 10$ . Hence, we can ignore the  $\Omega_{r,0}$  component as it is negligible at this redshift. Plugging this in  $\rho_{\text{int}}$ , we get,

$$\rho_{\text{int}}(z_0) = \frac{c \rho_{\text{crit}} \Omega_{m,0}}{H_0} \int_{z=0}^{z=z_0} \left( \frac{(1+z)^2}{\sqrt{\Omega_{m,0} (1+z)^3 + \Omega_{\Lambda,0}}} \right) dz. \quad (6.28)$$

In fig.(6.2.1), we have numerically evaluated the integral for

$$\rho_{\text{crit}} = 2.2 \times 10^{-27} \text{ kg m}^{-3}, \quad \Omega_{m,0} = 0.3, \quad (6.29)$$

and plotted it for different values of  $z_0$ .

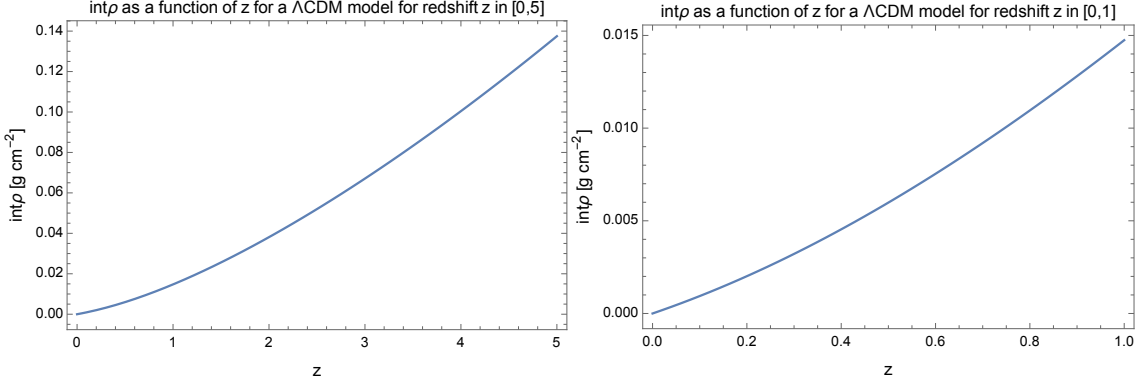


Figure 6.5: *Left:* Integrated dark matter column density from redshift  $z \in [0, 1]$  in an expanding  $\Lambda$ CDM universe ; *Right:* Integrated dark matter column density from redshift  $z \in [0, 5]$  in an expanding  $\Lambda$ CDM universe

At  $z = 1$ , we get a  $\rho_{\text{int}}$  comparable but less than corresponding to Milky

Ways's NFW dark matter halo (same order of magnitude),

$$\rho_{\text{int}}(z_0 = 1 \rightarrow 0) = 0.015 \text{ g cm}^{-3}. \quad (6.30)$$

### 6.2.2 Dwarf Galaxy

To compute the forwardschein from dwarf galaxies, we would first like to have their density profile. We use parameters from article [57] to model the density profile and reproduce some of the plots and results. We chose Leo I as the dwarf galaxy for our analysis. We adopt a generalized Hernquist profile like in the cited article,

$$\rho_{\text{DM}}(R, z) = \rho_0 \left( \frac{r}{b_{\text{halo}}} \right)^{-\gamma} \left[ 1 + \left( \frac{r}{b_{\text{halo}}} \right)^{\alpha} \right]^{-\frac{\beta-\gamma}{\alpha}}, \quad (6.31)$$

$$r^2 = R^2 + \frac{z^2}{Q^2}, \quad (6.32)$$

where  $\rho_0$  and  $b_{\text{halo}}$  are the scale density and radius, respectively,  $\alpha$  is the sharpness parameter of the transition from the inner slope  $\gamma$  to the outer slope  $\beta$ , and  $Q$  is a constant axial ratio of a dark matter halo. From the above-cited article, we have the following parameters,

$$Q = 1.39, \quad b_{\text{halo}} = 10^{3.5} \text{ pc}, \quad \rho_0 = 10^{-2.35} M_{\odot} \text{pc}^{-3}, \quad (6.33)$$

$$\alpha = 1.68, \quad \beta = 6.17, \quad \gamma = 1.35. \quad (6.34)$$

Using these estimates, we plot the Hernquist profile for LeoI,

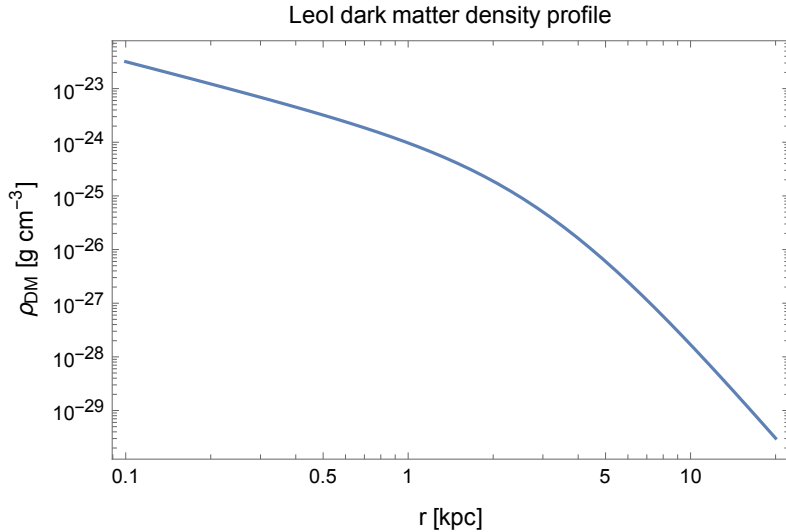


Figure 6.6: Dark matter density profile of dwarf galaxy Leo I plotted as a function of distance from the center of the halo

The astrophysical D factor for Leo I integrated over a solid angle of 0.5 is

given by  $D_{0.5} = 10^{17.6}$  GeV cm $^{-2}$ , where (For an upper bound, we assume  $\rho$  to be only radially dependent),

$$D_{0.5} = \int_0^{2\pi} d\phi \int_0^{0.5^\circ} \sin(\alpha) d\alpha \int_{\text{los}} \rho_{DM}(x) dx. \quad (6.35)$$

This gives us,

$$\rho_{\text{int}}(\text{LeoI}) = \int_{\text{los}} \rho_{DM}(x) dx = \frac{D_{0.5^\circ}}{2\pi \int_0^{0.5^\circ} \sin(\alpha) d\alpha} \quad (6.36)$$

$$= 0.0029 \text{ g cm}^{-2}. \quad (6.37)$$

### 6.3 Projected SNR

We combine the results from the three regions to estimate an axion forwardschein signal stimulated from a radio galaxy source piercing through an axion dark matter column made of: average cosmological dark matter from  $z = 1 \rightarrow 0$ , plus dark matter in LeoI, plus in Milky Way's dark matter halo.

We estimate the SNR using Five-hundred-meter Aperture Spherical Telescope (FAST),

$$\text{SNR(FAST)} = \frac{P_{\text{signal}}}{P_{\text{noise}}} = \frac{\hbar c^4 g_{a\gamma\gamma}^2}{16} \frac{S_{\nu\text{cygnus}}(\nu = 300 \text{ MHz}) \rho_{\text{int-total}} A_{\text{eff}}}{P_{\text{noise}}}, \quad (6.38)$$

where  $P_{\text{signal}}$  is the power in the forwardschein signal. The noise is given by [13],

$$P_{\text{noise}} = 2k_B T_{\text{sys}} \sqrt{\frac{\nu_{\text{ref}}/1000}{t_{\text{obs}}}}. \quad (6.39)$$

Using  $\nu_{\text{ref}} = 300 \text{ MHz}$ ,  $t_{\text{obs}} = 100 \text{ h}$  and a low  $T_{\text{sys}} = 30 \text{ K}$  in order to estimate the upper bound on SNR,

$$P_{\text{noise}} = 7.56 \times 10^{-15} \text{ g cm}^2 \text{ s}^{-3}. \quad (6.40)$$

The sum of integrated axion DM column over the three regions is given by,

$$\rho_{\text{int-total}} = \rho_{\text{int}}(z = 1 \rightarrow 0) + \rho_{\text{int}}(\text{LeoI}) + \rho_{\text{int}}(\text{MW}) \quad (6.41)$$

$$= (0.015 + 0.003 + 0.032) \text{ g cm}^{-2} = 0.05 \text{ g cm}^{-2} \quad (6.42)$$

$$= 0.5 \text{ kg m}^{-2}. \quad (6.43)$$

The source flux density is given by eq.(6.13) (plotted in fig.(6.4)), at  $\nu = 300 \text{ MHz}$  we have,

$$S_{\nu\text{cygnus}}(\nu = 300 \text{ MHz}) = 5.43 \times 10^{-24} \text{ g s}^{-2} = 0.54 \text{ Jy} \quad (6.44)$$

$$= 5.43 \times 10^{-27} \text{ W m}^{-2} \text{ Hz}^{-1}. \quad (6.45)$$

Carefully plugging all the quantities mentioned above into eq.(6.38) and en-

suring we get a dimensionless ratio, we get,

$$\text{SNR(FAST)} = 2.3 \times 10^{-4}. \quad (6.46)$$

## Conclusion

The SNR for a forwardschein signal for this slightly complex yet innovative case is very low. We do not expect any signature of forwardschein photons from past and present data that FAST has collected.

# Chapter 7

## Conclusion

This thesis studied the probability of detecting photons produced from decaying axions in the stellar basins of various compact astrophysical objects and in the Milky Way's dark matter halo. In particular, we look for photons produced from a stimulated decay of axions.

In chapter 2, we begin by briefly explaining the strong CP problem that motivates the existence of QCD axions. Further, we motivate the existence of ALPs. Then, with the help of appendix A, we show that axions can be produced via non-thermal means by the misalignment mechanism. This motivates the candidacy of axions as a dark matter candidate. We end the chapter by summarizing the various types of experiments searching for these particles.

In chapter 3, we established that, given an axion-photon interaction, a photon with an angular frequency half the axion's mass could produce a stimulated decay of the axion into two back-to-back photons. This is extremely crucial, as the vacuum lifetime of axions corresponds to time scales larger than the universe's age. The stimulated decay enables us to probe the axion-photon coupling in this scenario. In appendix B, we derive the Axion-Maxwell's equations. Using them, in appendix C we derive the power in the echo wave eq.(C.29) - electromagnetic wave corresponding to the photons when a density of axions goes under stimulated decay due to an external light source. This enables us to define the flux in a gegenschein or forwardschein signal produced from an axion source given in eq.(3.4).

In chapter 4, we dive deep into the details of the formalism that enables us to compute the properties of stellar basins. First, we motivate the existence of stellar basins. Then we derive a generic expression that enables us to estimate the injection rate of particles that enter a gravitationally bound orbit around a compact stellar object in eq.(4.18). This expression is a function of the emission rates of particles, which depend on their emission process. Using this expression, we compute the bound energy in the stellar basin for axions produced by the sun via axion-bremsstrahlung and axion-Compton scattering processes. The emission rate for axion-bremsstrahlung is derived in appendix D. The fig.(4.4)

has the axion energy density at Earth's surface from the solar basin plotted as a function of axion mass.

In chapter 5, we combine the ideas from the previous two chapters and look for axion echos in the solar axion basin and basins of other compact stellar objects like a white dwarf and a neutron star. We assume that the white dwarf and neutron star axion basin is highly similar to the solar axion basin. This is a simplifying assumption on the white dwarf and neutron star axion basin to make zeroth order estimates on the echo signal. Future studies that precisely compute axion stellar basins of a white dwarf and neutron stars could lead to different axion basin densities. Compared to our zeroth order assumptions, these results could potentially result in varied estimates for the echo signals.

- In section 5.1, we look for echos from basins formed out of 3 keV axions around the sun, white dwarf, and neutron stars; this is because the axion basin density is peaked at this axion mass. Photons from each of the mentioned stellar objects are used as the source of electromagnetic waves that boost the decay rates of the axions in their respective basins. We use the Chandra X-Ray telescope to estimate the SNR for the echo signals. We conclude that the axion echo signals from these basins in the X-ray domain are negligible.
- In section 5.2, we look for basinschein signals from the solar axion basin stimulated by the sun's UV, optical, and IR spectrum. We use different detectors on the HST to estimate flux ratios for the forwardschein signals. In all three scenarios, we find both the forwardschein and gegenschein signals feeble to be detected by HST.
- In section 5.3, we make a quick comparison between the flux densities emitted from an O-star and the sun. We assume that the O-star has a blackbody spectrum corresponding to  $T = 50000$  K. We conclude that any forwardschein estimates from the O-star will be more significant than the sun but in no way sufficient to produce a detectable signal.

Finally, in chapter 6, we estimate the axion echo by assuming that the dark matter halo of the Milky Way is entirely made out of axions. We call this axion haloschein.

- In section 6.1, we compute the haloschein signal by using an optical band from the sun as the stimulating source. We use HST to estimate the SNR ratio. Initially, we found a good SNR for an exposure time of 100 h. Unfortunately, our optimistic signal turns extremely weak after considering the dark current noise, as explained in appendix E. We perform precise calculations to estimate an upper bound on the SNR and find it too low to be detected by HST.

- In section 6.2, we assume a hypothetical scenario that the flux from a powerful radio galaxy at redshift one pierces through various regions containing dark matter axion densities, producing a forwardschein signal. In particular, it pierces through three regions, (i) the average dark matter density in space from  $z = 1$  to  $z = 0$  in an expanding FLRW universe, (ii) the dark matter density from a dwarf galaxy at the edge of our Milky Way, (iii) the dark matter density from the Milky Way's dark matter halo. We compute the required integrated axion densities for each of these regions. We assume that the radio galaxy has a spectrum similar to Cygnus A (one of the brightest radio galaxies). We tie all of this together, and unfortunately, we still find the SNR for this forwardschein signal to be extremely weak to be detected by FAST.

Our thesis aimed to put a new astrophysical bound on the axion-photon coupling by probing axion echos. In this thesis, we considered many scenarios that could produce axion echos. Unfortunately, the axion echo estimated from all these situations is too weak to constrain the axion-photon coupling further.

# Bibliography

- [1] R. D. Peccei and Helen R. Quinn. CP Conservation in the Presence of Instantons. *Phys. Rev. Lett.*, 38:1440–1443, 1977. [doi:10.1103/PhysRevLett.38.1440](https://doi.org/10.1103/PhysRevLett.38.1440).
- [2] P. Sikivie. Experimental Tests of the Invisible Axion. *Phys. Rev. Lett.*, 51:1415–1417, 1983. [Erratum: Phys.Rev.Lett. 52, 695 (1984)]. [doi:10.1103/PhysRevLett.51.1415](https://doi.org/10.1103/PhysRevLett.51.1415).
- [3] P. Sikivie. Detection rates for "invisible"-axion searches. *Phys. Rev. D*, 32:2988–2991, Dec 1985. URL: <https://link.aps.org/doi/10.1103/PhysRevD.32.2988>, [doi:10.1103/PhysRevD.32.2988](https://doi.org/10.1103/PhysRevD.32.2988).
- [4] Lawrence Krauss, John Moody, Frank Wilczek, and Donald E. Morris. Calculations for Cosmic Axion detection. *Phys. Rev. Lett.*, 55:1797–1800, Oct 1985. URL: <https://link.aps.org/doi/10.1103/PhysRevLett.55.1797>, [doi:10.1103/PhysRevLett.55.1797](https://doi.org/10.1103/PhysRevLett.55.1797).
- [5] Michael S. Turner. Early-Universe Thermal Production of Not-So-Invisible Axions. *Phys. Rev. Lett.*, 59:2489–2492, Nov 1987. URL: <https://link.aps.org/doi/10.1103/PhysRevLett.59.2489>, [doi:10.1103/PhysRevLett.59.2489](https://doi.org/10.1103/PhysRevLett.59.2489).
- [6] P. Sikivie and Q. Yang. Bose-Einstein Condensation of Dark Matter Axions. *Phys. Rev. Lett.*, 103:111301, 2009. [arXiv:0901.1106](https://arxiv.org/abs/0901.1106), [doi:10.1103/PhysRevLett.103.111301](https://doi.org/10.1103/PhysRevLett.103.111301).
- [7] Raymond T. Co and Keisuke Harigaya. Axiogenesis. *Phys. Rev. Lett.*, 124:111602, Mar 2020. URL: <https://link.aps.org/doi/10.1103/PhysRevLett.124.111602>, [doi:10.1103/PhysRevLett.124.111602](https://doi.org/10.1103/PhysRevLett.124.111602).
- [8] G. G. Raffelt. *Stars as laboratories for fundamental physics: The astrophysics of neutrinos, axions, and other weakly interacting particles*. 5 1996.
- [9] Ken Van Tilburg. Stellar basins of gravitationally bound particles. *Phys. Rev. D*, 104(2):023019, 2021. [arXiv:2006.12431](https://arxiv.org/abs/2006.12431), [doi:10.1103/PhysRevD.104.023019](https://doi.org/10.1103/PhysRevD.104.023019).

- [10] Matthew D. Schwartz. *Quantum Field Theory and the Standard Model*. Cambridge University Press, 3 2014.
- [11] Ariel Arza and Pierre Sikivie. Production and Detection of an Axion Dark Matter Echo. *Phys. Rev. Lett.*, 123:131804, Sep 2019. URL: <https://link.aps.org/doi/10.1103/PhysRevLett.123.131804>, doi: [10.1103/PhysRevLett.123.131804](https://doi.org/10.1103/PhysRevLett.123.131804).
- [12] Andrea Caputo, Marco Regis, Marco Taoso, and Samuel J. Witte. Detecting the Stimulated Decay of Axions at RadioFrequencies. *JCAP*, 03:027, 2019. [arXiv:1811.08436](https://arxiv.org/abs/1811.08436), doi: [10.1088/1475-7516/2019/03/027](https://doi.org/10.1088/1475-7516/2019/03/027).
- [13] Yitian Sun, Katelyn Schutz, Anjali Nambrath, Calvin Leung, and Kiyoshi Masui. Axion dark matter-induced echo of supernova remnants. *Phys. Rev. D*, 105(6):063007, 2022. [arXiv:2110.13920](https://arxiv.org/abs/2110.13920), doi: [10.1103/PhysRevD.105.063007](https://doi.org/10.1103/PhysRevD.105.063007).
- [14] Manuel A. Buen-Abad, JiJi Fan, and Chen Sun. Axion echoes from the supernova graveyard. *Phys. Rev. D*, 105:075006, Apr 2022. URL: <https://link.aps.org/doi/10.1103/PhysRevD.105.075006>, doi: [10.1103/PhysRevD.105.075006](https://doi.org/10.1103/PhysRevD.105.075006).
- [15] Michael E. Peskin and Daniel V. Schroeder. *An Introduction to quantum field theory*. Addison-Wesley, Reading, USA, 1995.
- [16] CPT symmetry structure of a Neutron.
- [17] Anson Hook. TASI Lectures on the Strong CP Problem and Axions, 2018. URL: <https://arxiv.org/abs/1812.02669>, doi: [10.48550/ARXIV.1812.02669](https://doi.org/10.48550/ARXIV.1812.02669).
- [18] Tom Lancaster and Stephen J. Blundell. *Quantum Field Theory for the Gifted Amateur*. Oxford University Press, 2014.
- [19] Andreas Pargner. *Phenomenology of Axion Dark Matter*. PhD thesis, KIT, Karlsruhe, IKP, 2 2019. doi: [10.5445/IR/1000092362](https://doi.org/10.5445/IR/1000092362).
- [20] David J. E. Marsh. Axion Cosmology. *Phys. Rept.*, 643:1–79, 2016. [arXiv:1510.07633](https://arxiv.org/abs/1510.07633), doi: [10.1016/j.physrep.2016.06.005](https://doi.org/10.1016/j.physrep.2016.06.005).
- [21] A P Zhitnitskii. Possible suppression of axion-hadron interactions. *Sov. J. Nucl. Phys. (Engl. Transl.); (United States)*. URL: <https://www.osti.gov/biblio/7063072>.
- [22] Michael Dine, Willy Fischler, and Mark Srednicki. A simple solution to the strong cp problem with a harmless axion. *Physics Letters B*, 104(3):199–202, 1981. URL: <https://www.sciencedirect.com/>

[science/article/pii/0370269381905906](https://science.org/doi/10.1103/0370269381905906), doi:<https://doi.org/10.1103/0370269381905906>.

- [23] Jihn E. Kim. Weak-interaction singlet and strong CP invariance. *Phys. Rev. Lett.*, 43:103–107, Jul 1979. URL: <https://link.aps.org/doi/10.1103/PhysRevLett.43.103>, doi:[10.1103/PhysRevLett.43.103](https://doi.org/10.1103/PhysRevLett.43.103).
- [24] Mikhail A. Shifman, A. I. Vainshtein, and Valentin I. Zakharov. Can Confinement Ensure Natural CP Invariance of Strong Interactions? *Nucl. Phys. B*, 166:493–506, 1980. doi:[10.1016/0550-3213\(80\)90209-6](https://doi.org/10.1016/0550-3213(80)90209-6).
- [25] Asimina Arvanitaki, Savas Dimopoulos, Sergei Dubovsky, Nemanja Kaloper, and John March-Russell. String Axiverse. *Phys. Rev. D*, 81:123530, Jun 2010. URL: <https://link.aps.org/doi/10.1103/PhysRevD.81.123530>, doi:[10.1103/PhysRevD.81.123530](https://doi.org/10.1103/PhysRevD.81.123530).
- [26] Notes taken during "Dark Matter Theory" course taken at Heidelberg University, Germany (Unpublished).
- [27] Nikita Blinov, Matthew J Dolan, Patrick Draper, and Jonathan Kozaczuk. Dark matter targets for axionlike particle searches. *Phys. Rev. D*, 100(1):015049, 2019. arXiv:1905.06952, doi:[10.1103/PhysRevD.100.015049](https://doi.org/10.1103/PhysRevD.100.015049).
- [28] Igor G. Irastorza and Javier Redondo. New experimental approaches in the search for axion-like particles. *Prog. Part. Nucl. Phys.*, 102:89–159, 2018. arXiv:1801.08127, doi:[10.1016/j.ppnp.2018.05.003](https://doi.org/10.1016/j.ppnp.2018.05.003).
- [29] C. B. Adams et al. Axion Dark Matter. In *2022 Snowmass Summer Study*, 3 2022. arXiv:2203.14923.
- [30] S. J. Asztalos, G. Carosi, C. Hagmann, D. Kinion, K. van Bibber, M. Hotz, L. J Rosenberg, G. Rybka, J. Hoskins, J. Hwang, P. Sikivie, D. B. Tanner, R. Bradley, and J. Clarke. SQUID-Based Microwave Cavity Search for Dark-Matter Axions. *Physical Review Letters*, 104(4), jan 2010. URL: <https://doi.org/10.1103/physrevlett.104.041301>, doi:[10.1103/physrevlett.104.041301](https://doi.org/10.1103/physrevlett.104.041301).
- [31] Ciaran O'Hare. cajohare/AxionLimits: AxionLimits. <https://cajohare.github.io/AxionLimits/>, July 2020. doi:[10.5281/zenodo.3932430](https://doi.org/10.5281/zenodo.3932430).
- [32] P. Brun et al. A new experimental approach to probe QCD Axion Dark Matter in the mass range above 40  $\mu$ eV. 3 2017.

- [33] Allen Caldwell, Gia Dvali, Béla Majorovits, Alexander Millar, Georg Raffelt, Javier Redondo, Olaf Reimann, Frank Simon, and Frank Steffen. Dielectric Haloscopes: A New Way to Detect Axion Dark Matter. *Phys. Rev. Lett.*, 118:091801, Mar 2017. URL: <https://link.aps.org/doi/10.1103/PhysRevLett.118.091801>, doi:10.1103/PhysRevLett.118.091801.
- [34] Oindrila Ghosh, Jordi Salvado, and Jordi Miralda-Escudé. Axion Gengenschein: Probing Back-scattering of Astrophysical Radio Sources Induced by Dark Matter. 8 2020. arXiv:2008.02729.
- [35] L DiLella and K Zioutas. Observational evidence for gravitationally trapped massive axion(-like) particles. *Astropart. Phys.*, 19:145–170, 2003. arXiv: astro-ph/0207073, doi:10.1016/S0927-6505(02)00186-X.
- [36] Robert Lasenby and Ken Van Tilburg. Dark photons in the Solar basin. , 104(2):023020, July 2021. arXiv:2008.08594, doi:10.1103/PhysRevD.104.023020.
- [37] William DeRocco, Shalma Wegsman, Brian Grefenstette, Junwu Huang, and Ken Van Tilburg. First Indirect Detection Constraints on Axions in the Solar Basin. *Phys. Rev. Lett.*, 129(10):101101, 2022. arXiv:2205.05700, doi: 10.1103/PhysRevLett.129.101101.
- [38] Asher Berlin and Katelin Schutz. Helioscope for gravitationally bound millicharged particles. *Phys. Rev. D*, 105(9):095012, 2022. arXiv:2111.01796, doi:10.1103/PhysRevD.105.095012.
- [39] H. Fischer, X. Liang, Y. Semertzidis, A. Zhitnitsky, and K. Zioutas. New mechanism producing axions in the AQN model and how the CAST can discover them. *Phys. Rev. D*, 98(4):043013, 2018. arXiv:1805.05184, doi: 10.1103/PhysRevD.98.043013.
- [40] Xunyu Liang and Ariel Zhitnitsky. Gravitationally bound axions and how one can discover them. *Phys. Rev. D*, 99(2):023015, 2019. arXiv:1810.00673, doi:10.1103/PhysRevD.99.023015.
- [41] Kyle Lawson, Xunyu Liang, Alexander Mead, Md Shahriar Rahim Siddiqui, Ludovic Van Waerbeke, and Ariel Zhitnitsky. Gravitationally trapped axions on the Earth. *Phys. Rev. D*, 100(4):043531, 2019. arXiv:1905.00022, doi:10.1103/PhysRevD.100.043531.
- [42] Georg G. Raffelt. Astrophysical axion bounds diminished by screening effects. *Phys. Rev. D*, 33:897–909, Feb 1986. URL: <https://link.aps.org/doi/10.1103/PhysRevD.33.897>, doi:10.1103/PhysRevD.33.897.

- [43] John N. Bahcall, Aldo M. Serenelli, and Sarbani Basu. New Solar Opacities, Abundances, Helioseismology, and Neutrino Fluxes. *The Astrophysical Journal*, 621(1):L85–L88, jan 2005. [doi:10.1086/428929](https://doi.org/10.1086/428929).
- [44] New CAST limit on the axion–photon interaction. *Nature Physics*, 13(6):584–590, may 2017. URL: <https://doi.org/10.1038%2Fnphys4109>, doi:10.1038/nphys4109.
- [45] M.F. Corcoran. X-Ray Astronomy. In Robert A. Meyers, editor, *Encyclopedia of Physical Science and Technology (Third Edition)*, pages 903–919. Academic Press, New York, third edition edition, 2003. URL: <https://www.sciencedirect.com/science/article/pii/B0122274105008292>, doi: <https://doi.org/10.1016/B0-12-227410-5/00829-2>.
- [46] Solar X-Ray flare Values. URL: <https://satdat.ngdc.noaa.gov/sem/goes/data/plots/special/>.
- [47] White Dwarf : KPD 0005+5106 Data. URL: <https://chandra.harvard.edu/photo/2021/kpd0005/>.
- [48] You-Hua Chu, Jesús A. Toalá, Martín A. Guerrero, Florian F. Bauer, Jana Bilikova, and Robert A. Gruendl. Hard X-Ray Emission Associated with White Dwarfs. IV. Signs of Accretion from Substellar Companions. *The Astrophysical Journal*, 910(2):119, apr 2021. URL: <https://doi.org/10.3847%2F1538-4357%2Fab5a5>, doi:10.3847/1538-4357/abe5a5.
- [49] T. Di Salvo, A. Santangelo, and A. Segreto. Hard X-ray emission from neutron star X-ray binaries. *Nuclear Physics B - Proceedings Supplements*, 132:446–455, 2004. Proceedings of the 2nd BeppoSAX Conference: The Restless High-Energy Universe. URL: <https://www.sciencedirect.com/science/article/pii/S0920563204001367>, doi:<https://doi.org/10.1016/j.nuclphysbps.2004.04.079>.
- [50] Kerstin Perez, Brandon Roach, Private communication.
- [51] Chandra X-Ray Telescope : High Resolution Mirror Assembly (HRMA) On-Axis effective area. URL: <https://cxc.harvard.edu/proposer/POG/html/chap4.html>.
- [52] Spectrum of Solar radiation on Earth.
- [53] Hubble Space Telescope’s media guide.
- [54] Hubble Space Telescope : SNR ratio formula.
- [55] Hubble Space Telescope’s online exposure time calculator. URL: <https://etc.stsci.edu/etc/input/stis/spectroscopic/>.

- [56] Scott Dodelson. *Modern Cosmology*. Academic Press, Amsterdam, 2003.
- [57] Kohei Hayashi, Masashi Chiba, and Tomoaki Ishiyama. *Astrophys. J.*, (1):45. [arXiv:2007.13780](https://arxiv.org/abs/2007.13780), doi:[10.3847/1538-4357/abbe0a](https://doi.org/10.3847/1538-4357/abbe0a).
- [58] Michael Dine and Willy Fischler. The not-so-harmless axion. *Physics Letters B*, 120(1):137–141, 1983. URL: <https://www.sciencedirect.com/science/article/pii/0370269383906391>, doi:[https://doi.org/10.1016/0370-2693\(83\)90639-1](https://doi.org/10.1016/0370-2693(83)90639-1).
- [59] John Preskill, Mark B. Wise, and Frank Wilczek. Cosmology of the invisible axion. *Physics Letters B*, 120(1):127–132, 1983. URL: <https://www.sciencedirect.com/science/article/pii/0370269383906378>, doi:[https://doi.org/10.1016/0370-2693\(83\)90637-8](https://doi.org/10.1016/0370-2693(83)90637-8).
- [60] Michael S. Turner. Coherent scalar-field oscillations in an expanding universe. *Phys. Rev. D*, 28:1243–1247, Sep 1983. URL: <https://link.aps.org/doi/10.1103/PhysRevD.28.1243>, doi:[10.1103/PhysRevD.28.1243](https://doi.org/10.1103/PhysRevD.28.1243).
- [61] Dark Currents. URL: <http://slittlefair.staff.shef.ac.uk/teaching/phy217/lectures/instruments/L11/index.html#semiconductors>.

# Appendix A

## FLRW axion misalignment

In this appendix we derive the equation of motion for the axion misalignment field in an expanding FLRW universe. We find that the expression we derived matches the one from standard literature [19, 58–60].

We have,

$$\mathcal{L}_\theta = f_a^2 \left[ -\frac{1}{2}(\partial_\mu \theta)(\partial^\mu \theta) - V(\theta) \right] \quad (\text{A.1})$$

$$V(\theta) = m_a^2 f_a^2 (1 - \cos \theta) \quad (\text{A.2})$$

The FLRW metric for a flat expanding universe ( $k = 0$ ) is given by,

$$ds^2 = dt^2 - R^2(t)d\vec{r}^2 \quad (\text{A.3})$$

In 1+3 Cartesian coordinates, we have,

$$g_{\mu\nu} = \begin{pmatrix} 1 & 0 & 0 & 0 \\ 0 & -R^2(t) & 0 & 0 \\ 0 & 0 & -R^2(t) & 0 \\ 0 & 0 & 0 & -R^2(t) \end{pmatrix} \quad (\text{A.4})$$

$$g^{\mu\nu} = \begin{pmatrix} 1 & 0 & 0 & 0 \\ 0 & -\frac{1}{R^2} & 0 & 0 \\ 0 & 0 & -\frac{1}{R^2} & 0 \\ 0 & 0 & 0 & -\frac{1}{R^2} \end{pmatrix} \quad (\text{A.5})$$

$$S_\theta = \int d^4x \sqrt{-g} \mathcal{L}_\theta \quad (\text{A.6})$$

The following is our Euler-Lagrange equation in curved spacetime where  $\nabla_\mu$  is the covariant derivative,

$$\frac{\partial \mathcal{L}_\theta}{\partial \theta} = \nabla_\mu \left( \frac{\partial \mathcal{L}_\theta}{\partial (\partial_\mu \theta)} \right) \quad (\text{A.7})$$

$$\text{LHS} = f_a^2 m_a^2 \sin \theta \quad (\text{A.8})$$

$$\text{RHS} = f_a^2 \nabla_\mu (g^{\mu\nu} \partial_\nu \theta) \quad (\text{A.9})$$

$$= f_a^2 g^{\mu\nu} \nabla_\mu (\partial_\nu \theta) \quad (\text{A.10})$$

$$\equiv f_a^2 \square \theta \quad (\text{A.11})$$

Evaluating the d'Alembertian,

$$\square \theta = g^{\mu\nu} \nabla_\mu (\partial_\nu \theta) \quad (\text{A.12})$$

$$= g^{\mu\nu} \left( \partial_\mu \partial_\nu \theta - \Gamma_{\mu\nu}^\alpha \partial_\alpha \theta \right) \quad (\text{A.13})$$

$$= g^{\mu\nu} \partial_\mu \partial_\nu \theta - g^{\mu\nu} \Gamma_{\mu\nu}^\alpha \partial_\alpha \theta \quad (\text{A.14})$$

$$= g^{00} \partial_0 \partial_0 \theta + g^{ij} \partial_i \partial_j \theta - g^{00} \Gamma_{00}^\alpha \partial_\alpha \theta - g^{ij} \Gamma_{ij}^\alpha \partial_\alpha \theta \quad (\text{A.15})$$

$$= \ddot{\theta} - \frac{1}{R^2} \nabla^2 \theta - (\Gamma_{00}^0 \partial_0 \theta + \Gamma_{00}^i \partial_i \theta) - g^{ij} (\Gamma_{ij}^0 \partial_0 \theta + \Gamma_{ij}^k \partial_k \theta) \quad (\text{A.16})$$

A quick Mathematica computation gives us the required Christoffel symbols,

$$\Gamma_{11}^0 = \Gamma_{22}^0 = \Gamma_{33}^0 = R(t) \dot{R}(t) \quad (\text{A.17})$$

$$\Gamma_{10}^1 = \Gamma_{01}^1 = \Gamma_{20}^2 = \Gamma_{02}^2 = \Gamma_{30}^3 = \Gamma_{03}^3 = \frac{\dot{R}(t)}{R(t)} \quad (\text{A.18})$$

giving us,

$$\square \theta = \ddot{\theta} - \frac{1}{R^2} \nabla^2 \theta + g^{ij} (\Gamma_{ij}^0 \partial_0 \theta - \Gamma_{ij}^k \partial_k \theta) \quad (\text{A.19})$$

$$= \ddot{\theta} - \frac{1}{R^2} \nabla^2 \theta - (g^{11} \Gamma_{11}^0 + g^{22} \Gamma_{22}^0 + g^{33} \Gamma_{33}^0) \partial_0 \theta \quad (\text{A.20})$$

$$- g^{ij} (\Gamma_{ij}^1 \partial_1 \theta + \Gamma_{ij}^2 \partial_2 \theta + \Gamma_{ij}^3 \partial_3 \theta) \quad (\text{A.21})$$

$$= \ddot{\theta} - \frac{1}{R^2} \nabla^2 \theta + 3 \frac{1}{R^2} (R \dot{R}) \dot{\theta} \quad (\text{A.21})$$

$$= \ddot{\theta} - \frac{1}{R^2} \nabla^2 \theta + 3 \frac{\dot{R}}{R} \dot{\theta} \quad (\text{A.22})$$

Defining Hubble rate as  $H = \dot{R}/R$ , we reach the following equation describing the action of the d'Alembertian operator on our axion (or misalignment) field  $\theta$ ,

$$\square \theta = \ddot{\theta} + 3H\dot{\theta} - \frac{1}{R^2} \nabla^2 \theta \quad (\text{A.23})$$

Equating LHS (A.8) = RHS (A.23) we get the following equation of motion for

the axion (or misalignment) field in an expanding FLRW universe,

$$\boxed{\left( \partial_t^2 + 3H\partial_t - \frac{\nabla^2}{R^2} \right) \theta + m_a(t)^2 \sin \theta = 0} \quad (\text{A.24})$$

# Appendix B

## Axion Electrodynamics

In this appendix, we will derive the modified Maxwell's equations for a model consisting of a standard massless  $U(1)$  boson and a massive pseudo-scalar particle  $a$  (axion). The boson and the pseudo-scalar interact via a  $aF_{\mu\nu}\tilde{F}^{\mu\nu}$  term. We get the same equations as in [2], which is the original paper that motivated and derived them.

### B.1 Axion Klein-Gordon equation

We can compute the modified Maxwell's equations for an additional axion field in a standard by starting from the following Lagrangian density,

$$\mathcal{L} = -\frac{1}{4}F^{\mu\nu}F_{\mu\nu} + \frac{1}{2}(\partial_\mu a)(\partial^\mu a) - \frac{1}{2}m_a^2a^2 + \frac{1}{4}g a F_{\mu\nu}\tilde{F}^{\mu\nu} \quad (\text{B.1})$$

where  $a$  is the axion field,  $m_a$  the mass of the axion,  $F^{\mu\nu}$  is the  $U(1)$  field strength tensor,  $\tilde{F}^{\mu\nu} = (1/2)\epsilon^{\mu\nu\alpha\beta}F_{\alpha\beta}$  it's dual, and  $g$  is the coupling constant for dimension five the operator that couples the axion to the photon (as seen in the last term). We can plug this Lagrangian into the Euler-Lagrange equations to get the necessary equations of motion which will be our modified Maxwell's equations, in the presence of an axion field.

$$\frac{\partial \mathcal{L}}{\partial a} = \partial_\alpha \left( \frac{\partial \mathcal{L}}{\partial (\partial_\alpha a)} \right) \quad (\text{B.2})$$

$$-m_a^2a + \frac{1}{4}g F_{\mu\nu}\tilde{F}^{\mu\nu} = \partial_\alpha \left( \frac{\partial}{\partial (\partial_\alpha a)} \left( \frac{1}{2}(\partial_\mu a)(\partial^\mu a) \right) \right) \quad (\text{B.3})$$

Carefully evaluating the  $\partial/(\partial(\partial_\alpha a))$  term in RHS, we get,

$$\frac{\partial}{\partial (\partial_\alpha a)} \left( \frac{1}{2}(\partial_\mu a)(\partial^\mu a) \right) = \frac{1}{2} \left( \frac{\partial(\partial_\mu a)}{\partial(\partial_\alpha a)}(\partial^\mu a) + (\partial_\mu a) \frac{\partial(\partial^\mu a)}{\partial(\partial_\alpha a)} \right) \quad (\text{B.4})$$

$$= \frac{1}{2} \left( \delta_{\mu\alpha} (\partial^\mu a) + (\partial_\mu a) g^{\mu\nu} \frac{\partial (\partial_\nu a)}{\partial (\partial_\alpha a)} \right) \quad (\text{B.5})$$

$$= \frac{1}{2} \left( (\partial^\alpha a) + (\partial_\mu a) \underbrace{g^{\mu\nu} \delta_{\nu\alpha}}_{g^{i\mu\alpha}} \right) \quad (\text{B.6})$$

$$= \frac{1}{2} (2\partial^\alpha a) = \partial^\alpha a \quad (\text{B.7})$$

Plugging this back into our equation, we get

$$-m_a^2 a + \frac{1}{4} g F_{\mu\nu} \tilde{F}^{\mu\nu} = \partial_\alpha (\partial^\alpha a) \quad (\text{B.8})$$

Rearranging this equation, we get

$$\boxed{(\partial^2 + m^2) a = \frac{1}{4} g F_{\mu\nu} \tilde{F}^{\mu\nu}} \quad (\text{B.9})$$

Which is similar to our well known Klein-Gordon wave equation,  $(\partial^2 + m^2) \psi(x) = J(x)$  where  $J(x)$  is the source term of the wave  $\psi(x)$ . Drawing an analogy to this, we can see that our axion field can be sourced by a  $F_{\mu\nu} \tilde{F}^{\mu\nu}$  term. We will further evaluate this source term into an even more familiar-looking expression as a function of  $\vec{E}$  and  $\vec{B}$ . The following algebra helps us reduce the  $F \tilde{F}$  term to a form that comes in handy several times.

$$F_{\mu\nu} \tilde{F}^{\mu\nu} = \frac{1}{2} \epsilon^{\mu\nu\alpha\beta} F_{\mu\nu} F_{\alpha\beta} \quad (\text{B.10})$$

$$= \frac{1}{2} \left( \epsilon^{0ijk} F_{0i} F_{jk} + \epsilon^{i0jk} F_{i0} F_{jk} + \epsilon^{ij0k} F_{ij} F_{0k} + \epsilon^{ijk0} F_{ij} F_{k0} \right) \quad (\text{B.11})$$

$$= \frac{1}{2} \left( (\epsilon^{0ijk} - \epsilon^{i0jk}) F_{0i} F_{jk} + (\epsilon^{ij0k} - \epsilon^{ijk0}) F_{0k} F_{ij} \right) \quad (\text{B.12})$$

$$= \frac{1}{2} \left( 2\epsilon^{0ijk} F_{0i} F_{jk} + 2\epsilon^{ij0k} F_{0k} F_{ij} \right) \quad (\text{B.13})$$

$$= \frac{1}{2} \left( 2\epsilon^{0ijk} F_{0i} F_{jk} + 2\epsilon^{jk0i} F_{0i} F_{jk} \right) \quad (\text{B.14})$$

$$= \frac{1}{2} \left( 2\epsilon^{0ijk} F_{0i} F_{jk} + 2\epsilon^{0ijk} F_{0i} F_{jk} \right) \quad (\text{B.15})$$

$$= 2 \left( \epsilon^{0ijk} F_{0i} F_{jk} \right) \quad (\text{B.16})$$

We can further expand this in terms of  $\vec{E}$  and  $\vec{B}$ , which will help us interpret the equations of motion from a canonical perspective. To do that, we will first expand the field strength tensors in terms of  $\vec{E}$  and  $\vec{B}$  by using the definition of  $F_{\mu\nu}$ ,

$$F_{0i} = -E_i \quad (\text{B.17})$$

$$F_{ij} = \epsilon_{ijk} B^k \quad (\text{B.18})$$

We can contract the indices on  $F\tilde{F}$  using the above two equations,

$$F_{\mu\nu}\tilde{F}^{\mu\nu} = 2 \left( \epsilon^{0ijk} F_{0i} F_{jk} \right) = -2 \left( \epsilon^{0ijk} E_i \epsilon_{jkl} B^l \right) \quad (\text{B.19})$$

$$= -2 \underbrace{\epsilon^{0ijk} \epsilon_{jkl}}_{2\delta_l^i} \left( E_i B^l \right) = -4 \left( \vec{E} \cdot \vec{B} \right) \quad (\text{B.20})$$

Using this, the axion Klein-Gordon equation reads as,

$$\boxed{\left( \partial^2 + m^2 \right) a = -g \left( \vec{E} \cdot \vec{B} \right)} \quad (\text{B.21})$$

## B.2 Axion Maxwell equation

To get our modified Maxwell equations, we want to minimize the action for  $\mathcal{L}$  with  $A_\alpha$ . Hence, we use the following Euler-Lagrange equation,

$$\frac{\partial \mathcal{L}}{\partial A_\alpha} = \partial_\lambda \left( \frac{\partial \mathcal{L}}{\partial (\partial_\lambda A_\alpha)} \right) \quad (\text{B.22})$$

Looking at the Lagrangian, we can easily see that the only term that will count as a modification to the regular Maxwell's equation is given by the  $F\tilde{F}$  term. Hence, we will compute the equation of motion for that term and add it to regular Maxwell's equation. Defining  $\mathcal{L} \supset \mathcal{L}_a = (1/4) g a F_{\mu\nu} \tilde{F}^{\mu\nu}$ , we have the LHS as,

$$\text{LHS} = \frac{\partial \mathcal{L}}{\partial A_\alpha} = 0 \quad (\text{B.23})$$

as there is no explicit  $A_\alpha$  dependence in  $\mathcal{L}_a$ .

$$\text{RHS} = -\frac{1}{2} \partial_\lambda F^{\lambda\alpha} + \partial_\lambda \left( \frac{\partial \mathcal{L}_a}{\partial (\partial_\lambda A_\alpha)} \right) \quad (\text{B.24})$$

$$= -\frac{1}{2} \partial_\lambda F^{\lambda\alpha} + \frac{1}{4} g \partial_\lambda \left( a \underbrace{\frac{\partial (F_{\mu\nu} \tilde{F}^{\mu\nu})}{\partial (\partial_\lambda A_\alpha)}}_{(*)} \right) \quad (\text{B.25})$$

evaluating the  $(*)$  term,

$$(*) \Rightarrow \left( \frac{\partial (F_{\mu\nu} \tilde{F}^{\mu\nu})}{\partial (\partial_\lambda A_\alpha)} \right) = \left( \frac{\partial ((\partial_\mu A_\nu - \partial_\nu A_\mu) \tilde{F}^{\mu\nu})}{\partial (\partial_\lambda A_\alpha)} \right) \quad (\text{B.26})$$

$$= \left( \frac{\partial ((\partial_\mu A_\nu - \partial_\nu A_\mu) \tilde{F}^{\mu\nu})}{\partial (\partial_\lambda A_\alpha)} \right) \quad (\text{B.27})$$

$$= \left( \delta_\mu^\lambda \delta_\nu^\alpha - \delta_\nu^\lambda \delta_\mu^\alpha \right) \tilde{F}^{\mu\nu} \quad (\text{B.28})$$

$$= \left( \tilde{F}^{\lambda\alpha} - \tilde{F}^{\alpha\lambda} \right) \quad (\text{B.29})$$

$$= 2\tilde{F}^{\lambda\alpha} \quad (\text{B.30})$$

gives us,

$$\text{RHS} = -\frac{1}{2}\partial_\lambda F^{\lambda\alpha} + \frac{1}{2}ga\partial_\lambda \left( a\tilde{F}^{\lambda\alpha} \right) \quad (\text{B.31})$$

gathering LHS=RHS, we get,

$$\partial_\lambda F^{\lambda\alpha} = g\partial_\lambda \left( a\tilde{F}^{\lambda\alpha} \right) \quad (\text{B.32})$$

$$\partial_\lambda F^{\lambda\alpha} = g \left( (\partial_\lambda a)\tilde{F}^{\lambda\alpha} + a(\partial_\lambda \tilde{F}^{\lambda\alpha}) \right) \quad (\text{B.33})$$

using  $\partial_\lambda \tilde{F}^{\lambda\alpha} = 0$  we get,

$$\boxed{\partial_\lambda F^{\lambda\alpha} = g(\partial_\lambda a)\tilde{F}^{\lambda\alpha}} \quad (\text{B.34})$$

Expanding for  $\alpha$ , we get the axion Maxwell's equations, starting with  $\alpha = 0$

$$\partial_\lambda F^{\lambda 0} = g(\partial_\lambda a)\tilde{F}^{\lambda 0} \quad (\text{B.35})$$

$$\partial_0 F^{00} + \partial_i F^{i0} = g \left( (\partial_0 a)\tilde{F}^{00} + (\partial_i a)\tilde{F}^{i0} \right) \quad (\text{B.36})$$

$$\partial_i F^{i0} = g(\partial_i a)\tilde{F}^{i0} \quad (\text{B.37})$$

$$= g(\partial_i a)\tilde{F}^{i0} \quad (\text{B.38})$$

which expanding  $\tilde{F}^{i0} = (1/2)\epsilon^{i0\alpha\beta}F_{\alpha\beta} = (1/2)\epsilon^{i0jk}F_{jk} = -(1/2)\epsilon^{0ijk}F_{jk} = B^i$

$$\partial_i F^{i0} = g(\partial_i a)B^i \quad (\text{B.39})$$

$$\boxed{\vec{\nabla} \cdot \vec{E} = g\vec{B} \cdot (\vec{\nabla} a)} \quad (\text{B.40})$$

Now, for  $\alpha = k$ ,

$$\partial_\lambda F^{\lambda k} = g(\partial_\lambda a)\tilde{F}^{\lambda k} \quad (\text{B.41})$$

$$\partial_0 F^{0k} + \partial_i F^{ik} = g \left( (\partial_0 a)\tilde{F}^{0k} + (\partial_i a)\tilde{F}^{ik} \right) \quad (\text{B.42})$$

$$= g \left( -(\partial_t a)B^k + \vec{E} \times \vec{\nabla} a \right) \quad (\text{B.43})$$

$$-\frac{\partial \vec{E}}{\partial t} + (\vec{\nabla} \times \vec{B}) = g \left( \vec{E} \times \vec{\nabla} a - \vec{B} \frac{\partial a}{\partial t} \right) \quad (\text{B.44})$$

$$\boxed{-\frac{\partial \vec{E}}{\partial t} + (\vec{\nabla} \times \vec{B}) = g \left( \vec{E} \times \vec{\nabla} a - \vec{B} \frac{\partial a}{\partial t} \right)} \quad (\text{B.45})$$

We can express this in terms of the magnetic vector potential  $\vec{A}$  which will serve as a starting point for the derivation in Appendix. (??)

$$\left( \frac{\partial^2 \vec{A}}{\partial t^2} + (\vec{\nabla}(\vec{\nabla} \cdot \vec{A}) - \nabla^2 A) \right) = g \left( -\frac{\partial \vec{A}}{\partial t} \times \vec{\nabla} a - (\vec{\nabla} \times \vec{A}) \frac{\partial a}{\partial t} \right) \quad (\text{B.46})$$

where if we choose Coulomb gauge,  $\vec{\nabla} \cdot \vec{A} = 0$ , we get

$$(\partial_t^2 - \nabla^2) \vec{A} = g \left( -\frac{\partial \vec{A}}{\partial t} \times \vec{\nabla} a - (\vec{\nabla} \times \vec{A}) \frac{\partial a}{\partial t} \right) \quad (\text{B.47})$$

# Appendix C

## Axion Echo

In this appendix, we derive the expression for the power in an axion echo. We successfully derive the expression following [11].

We assume a perfectly cold axion fluid of density  $\rho = (1/2) m_a^2 A^2$  where we define the axion field by  $\phi = A \sin(m_a t)$ . We have already chosen the Coulomb gauge while deriving the modified Axion-Maxwell equation, in which the second inhomogeneous Maxwell's equation in the presence of an axion field is given by Eq. (B.47) as seen in Appendix. (B),

$$(\partial_t^2 - \nabla^2) \vec{A} = -g (\vec{\nabla} \times \vec{A}) \partial_t \phi \quad (\text{C.1})$$

We start by considering vector potential for the incoming radiation that will stimulate the decay and another one for radiation/echo produced due to the decay. We will label them as  $\vec{A}_0$  and  $\vec{A}_1$  respectively. For,

$$\vec{A}_0(x, t) = \text{Re} \left( \int d^3k \vec{A}_0(\vec{k}) e^{i(\vec{k} \cdot \vec{x} - \omega t)} \right) \quad (\text{C.2})$$

Here  $\omega = |\vec{k}| = k$ . We can use  $\vec{A}_0$  as the source for production of  $\vec{A}_1$  in the presence of an axion density by using Eq.(C.1),

$$(\partial_t^2 - \nabla^2) \vec{A}_1 = -g (\vec{\nabla} \times \vec{A}_0) \partial_t \phi + \mathcal{O}(g^2) \quad (\text{C.3})$$

Where we can define  $\vec{A}_1$  as,

$$\vec{A}_1(\vec{x}, t) = \text{Re} \left( \int d^3k \vec{A}_1(\vec{k}, t) e^{i(\vec{k} \cdot \vec{x} + \omega t)} \right) \quad (\text{C.4})$$

Using Eq. (C.2), Eq. (C.4) in Eq. (C.3) and as we are working with the Fourier transform of our functions, we can always make the  $\vec{\nabla} \rightarrow i\vec{k}$  replacement,

$$\left(\partial_t^2 - \nabla^2\right) \left( \int d^3k A_1(\vec{k}, t) e^{i\vec{k}\cdot\vec{x} + \omega t} \right) \quad (C.5)$$

$$= -g \left( \vec{\nabla} \times \operatorname{Re} \left( \int d^3k \vec{A}_0(\vec{k}) e^{i(\vec{k}\cdot\vec{x} - \omega t)} \right) \right) \partial_t (A \sin(m_a t)) \\ \left( \partial_t^2 - i^2 k^2 \right) \left( \int d^3k A_1(\vec{k}, t) e^{i\vec{k}\cdot\vec{x} + \omega t} \right) \quad (C.6)$$

$$= -g A m_a \cos(m_a t) \left( i\vec{k} \times \left( \int d^3k \vec{A}_0(\vec{k}) e^{i(\vec{k}\cdot\vec{x} - \omega t)} \right) \right) \\ \left( \partial_t^2 + k^2 \right) \left( \int d^3k A_1(\vec{k}, t) e^{i\vec{k}\cdot\vec{x}} e^{i\omega t} \right) \quad (C.7)$$

$$= -g A m_a \cos(m_a t) \left( i\vec{k} \times \left( \int d^3k \vec{A}_0(\vec{k}) e^{i\vec{k}\cdot\vec{x}} e^{-i\omega t} \right) \right) \\ \left( \partial_t^2 + \omega^2 \right) \operatorname{Re} \left( \int d^3k A_1(\vec{k}, t) e^{i\omega t} \right) \\ = -g A m_a \cos(m_a t) \left( i\vec{k} \times \left( \int d^3k \vec{A}_0(\vec{k}) e^{-i\omega t} \right) \right) \quad (C.8)$$

$$\left( \partial_t^2 + \omega^2 \right) A_1(\vec{k}, t) e^{i\omega t} = -g A m_a \cos(m_a t) \left( i\vec{k} \times \vec{A}_0(\vec{k}) e^{-i\omega t} \right) \quad (C.9)$$

$$\left( \partial_t^2 + \omega^2 \right) A_1(\vec{k}, t) e^{i\omega t} = -g A m_a \left( \frac{e^{im_a t} + e^{-im_a t}}{2} \right) \left( i\vec{k} \times \vec{A}_0(\vec{k}) e^{-i\omega t} \right) \quad (C.10)$$

$$\left( \partial_t^2 + \omega^2 \right) A_1(\vec{k}, t) e^{i\omega t} = -\frac{g A m_a}{2} \left( i\vec{k} \times \vec{A}_0(\vec{k}) \right) e^{i(m_a - \omega)t} \quad (C.11)$$

We dropped the  $e^{-im_a t}$  term, which does not give any resonance.

$$\text{LHS} = \partial_t^2 \left( A_1(\vec{k}, t) e^{i\omega t} \right) + \omega^2 \left( A_1(\vec{k}, t) e^{i\omega t} \right) \quad (C.12)$$

$$= \partial_t \left( e^{i\omega t} \partial_t A_1(\vec{k}, t) + i\omega e^{i\omega t} A_1(\vec{k}, t) \right) + \omega^2 \left( A_1(\vec{k}, t) e^{i\omega t} \right) \quad (C.13)$$

$$= \left( \partial_t^2 A_1(\vec{k}, t) \right) e^{i\omega t} + i\omega e^{i\omega t} \partial_t \left( A_1(\vec{k}, t) \right) + \cancel{(i\omega)^2 \left( A_1(\vec{k}, t) e^{i\omega t} \right)} \\ + i\omega e^{i\omega t} \partial_t \left( A_1(\vec{k}, t) \right) + \cancel{\omega^2 \left( A_1(\vec{k}, t) e^{i\omega t} \right)} \quad (C.14)$$

$$= \left( \partial_t^2 A_1(\vec{k}, t) \right) e^{i\omega t} + 2i\omega e^{i\omega t} \partial_t A_1(\vec{k}, t) \quad (C.15)$$

Plugging this back into our equation gives us,

$$\left( \partial_t^2 A_1(\vec{k}, t) \right) e^{i\omega t} + 2i\omega e^{i\omega t} \partial_t A_1(\vec{k}, t) = -\frac{g A m_a}{2} \left( i\vec{k} \times \vec{A}_0(\vec{k}) \right) e^{i(m_a - \omega)t} \quad (C.16)$$

$$\left(\partial_t^2 A_1(\vec{k}, t)\right) + 2i\omega \partial_t A_1(\vec{k}, t) = -\frac{gAm_a}{2} \left(i\vec{k} \times \vec{A}_0(\vec{k})\right) e^{i(m_a-2\omega)t} \quad (\text{C.17})$$

We ignore the  $\partial_t^2$  term compared to the  $\partial_t$  term by assuming slowly varying  $\vec{A}_1$  concerning time. This gives us,

$$\left(\partial_t^2 A_1(\vec{k}, t)\right) + 2i\omega \partial_t A_1(\vec{k}, t) = -\frac{gAm_a}{2} \left(i\vec{k} \times \vec{A}_0(\vec{k})\right) e^{i(m_a-2\omega)t} \quad (\text{C.18})$$

$$\partial_t A_1(\vec{k}, t) = -\frac{gAm_a}{4\omega} \left(i\vec{k} \times \vec{A}_0(\vec{k})\right) e^{i(m_a-2\omega)t} \quad (\text{C.19})$$

We can solve this differential equation with ease by assuming  $\vec{A}_1(\vec{k}, 0) = 0$

$$\int_0^t \partial_{t'} \vec{A}_1(\vec{k}, t') dt' = -\frac{gAm_a}{4\omega} \left(i\vec{k} \times \vec{A}_0(\vec{k})\right) \int_0^t e^{i(m_a-2\omega)t'} dt' \quad (\text{C.20})$$

$$\vec{A}_1(\vec{k}, t) = -\frac{gAm_a}{4\omega} \left(i\vec{k} \times \vec{A}_0(\vec{k})\right) \left( \frac{e^{i(m_a-2\omega)t} - 1}{i(m_a - 2\omega)} \right) \quad (\text{C.21})$$

We can redefine  $\epsilon = m_a/2 - \omega$ , to have,

$$\vec{A}_1(\vec{k}, t) = -\frac{gAm_a}{4\omega} \left(i\vec{k} \times \vec{A}_0(\vec{k})\right) \left( \frac{e^{i2\epsilon t} - 1}{2i\epsilon} \right) \quad (\text{C.22})$$

$$= -\frac{gAm_a}{4\omega} \left(i\vec{k} \times \vec{A}_0(\vec{k})\right) e^{i\epsilon t} \left( \frac{e^{i\epsilon t} - e^{-i\epsilon t}}{2i\epsilon} \right) \quad (\text{C.23})$$

$$= -\frac{gAm_a}{4\omega} \left(i\vec{k} \times \vec{A}_0(\vec{k})\right) e^{i\epsilon t} \left( \frac{\sin(\epsilon t)}{\epsilon} \right) \quad (\text{C.24})$$

From here, we can compute the power in the  $\vec{A}_1$  wave as a function of power in  $\vec{A}_0$  wave. We define the power in the  $\vec{A}_0$  wave as

$$P_0 = \int d\omega \frac{dP_0}{d\omega} \quad (\text{C.25})$$

Using this and the fact that

$$\lim_{t \rightarrow \infty} \left( \frac{\sin(\epsilon t)}{\epsilon} \right)^2 = \delta(\epsilon) \pi t \quad (\text{C.26})$$

Plugging these in, we get the power for  $\vec{A}_1$ ,

$$P_1 = \frac{g^2 A^2 m_a^2}{16} \hat{k}^2 P_0 \left( \frac{\sin(\epsilon t)}{\epsilon} \right)^2 \quad (\text{C.27})$$

where  $\hat{k} = \vec{k}/\omega$ .

$$P_1 = \frac{g^2 A^2 m_a^2 t}{16} \int d\omega \frac{dP_0}{d\omega}(\omega) \delta\left(\frac{m_a}{2} - \omega\right) \pi \quad (\text{C.28})$$

$$= \frac{g^2 \rho}{16} \left[ \frac{dP_0}{d\omega} \right]_{\omega=\frac{m_a}{2}} \pi t \quad (C.29)$$

## Appendix D

# Energy loss rate for axion production via axion-bremstrahlung

In this appendix, we compute the expression for the energy loss rate of an axion produced from an axion-bremstrahlung process. We successfully derive the expression given in [9] upto a factor of four.

We start with eq.(4.19) for axion bremstrahlung, where the variables are defined according to fig.(4.2),

$$Q_B = \frac{1}{(2\pi)^3} \int \frac{d^3 k}{2} \underbrace{\left( \frac{g_1 g_2}{(2\pi)^6} \frac{1}{4} \int \frac{d^3 p_1}{E_1} \int \frac{d^3 p_2}{E_2} \right)}_{\mathbb{P}_{\text{in}}} \\ \underbrace{\left( \frac{g_3 g_4}{(2\pi)^6} \frac{1}{4} \int \frac{d^3 p_3}{E_3} \int \frac{d^3 p_4}{E_4} \right)}_{\mathbb{P}_{\text{out}}} \underbrace{\frac{Z_j^2 e^4 g_{aee}^2 4m_j^2}{|\vec{q}^2 + \kappa_s^2 m_e^2}}_{|\mathcal{M}|^2} \\ (2\pi)^4 \delta^3(\vec{p}_1 + \vec{p}_2 - \vec{p}_3 - \vec{p}_4 - \vec{k}) \delta(E_1 + E_2 - E_3 - E_4 - \omega) \mathbb{F} \quad (\text{D.1})$$

We can now define  $\vec{q} := \vec{p}_2 - \vec{p}_4$ . We can also break down the Dirac delta function as follows,

$$\delta^3(\vec{p}_1 + \vec{p}_2 - \vec{p}_3 - \vec{p}_4 - k) = \int d^3 q \delta^3(\vec{p}_1 - \vec{p}_3 - k + \vec{q}) \delta^3(\vec{q} - \vec{p}_2 + \vec{p}_4) \quad (\text{D.2})$$

Plugging this into  $Q_B$  (equation bleeds onto next page),

$$Q_B = \frac{4g_1 g_2 g_3 g_4}{32(2\pi)^{11}} \frac{Z_j^2 e^4 g_{aee}^2 m_j^2}{m_e^2} \int d^3 k$$

$$\begin{aligned}
& \int \frac{d^3 p_1}{\left(m_e + \frac{\vec{p}_1^2}{2m_e}\right)} \int \frac{d^3 p_2}{m_j} \int \frac{d^3 p_3}{\left(m_e + \frac{\vec{p}_3^2}{2m_e}\right)} \int \frac{d^3 p_4}{m_j} \\
& \int d^3 q \delta^3(\vec{p}_1 - \vec{p}_3 - \vec{k} + \vec{q}) \delta^3(\vec{q} - \vec{p}_2 + \vec{p}_4) \\
& \delta \left( \frac{\vec{p}_1^2 - \vec{p}_3^2}{2m_e} - \omega \right) \frac{1}{\vec{q}^2 + \kappa_s^2} \mathbb{F}
\end{aligned} \tag{D.3}$$

where we have used  $E_{1,3} = m_e + (\vec{p}_{1,3}^2/2m_e)$  and  $E_2 = E_4 = m_j$ . We can also safely assume  $m_e \gg \vec{p}_1, \vec{p}_2$ , which will give us  $m_e + \vec{p}_{1,3}^2/2m_e \rightarrow m_e$  (Except inside the Dirac delta function, the  $m_e$ 's cancel each other). Applying these approximations we have,

$$\begin{aligned}
Q_B = & \frac{4g_1g_2g_3g_4}{32(2\pi)^{11}} \frac{Z_j^2 e^4 g_{aee}^2}{m_e^4} \int d^3 k \int d^3 p_1 \int d^3 p_2 \int d^3 p_3 \int d^3 p_4 \\
& \int d^3 q \delta^3(\vec{p}_1 - \vec{p}_3 - \vec{k} + \vec{q}) \delta^3(\vec{q} - \vec{p}_2 + \vec{p}_4) \\
& \delta \left( \frac{\vec{p}_1^2 - \vec{p}_3^2}{2m_e} - \omega \right) \frac{1}{\vec{q}^2 + \kappa_s^2} \mathbb{F}
\end{aligned} \tag{D.4}$$

We integrate out  $d^3 p_4$  over  $\delta^3(\vec{q} - \vec{p}_2 + \vec{p}_4)$ . There is no  $\vec{p}_4$  dependence in our expression, so this integral fixes  $\vec{q} = \vec{p}_2 - \vec{p}_4$  as we had defined (The main purpose of this step is to get a  $\int d^3 \vec{q}$  in our expression as the propagator explicitly depends on it). Also, in the soft limit we take  $\vec{k} \rightarrow 0, \omega \rightarrow m$ ,

$$\begin{aligned}
Q_B = & \frac{4g_1g_2g_3g_4}{32(2\pi)^{11}} \frac{Z_j^2 e^4 g_{aee}^2}{m_e^4} \int d^3 k \int d^3 p_1 \int d^3 p_2 \int d^3 p_3 \int d^3 q \\
& \delta^3(\vec{p}_1 - \vec{p}_3 + \vec{q}) \delta \left( \frac{\vec{p}_1^2 - \vec{p}_3^2}{2m_e} - m \right) \frac{1}{\vec{q}^2 + \kappa_s^2} \mathbb{F}
\end{aligned} \tag{D.5}$$

Where we have the distribution factor as (where  $f = f(k)$  for the axion),

$$\mathbb{F} = (1+f) \mathbb{F}_{in} \bar{\mathbb{F}}_{out} - f \mathbb{F}_{out} \bar{\mathbb{F}}_{in} \tag{D.6}$$

$$= (1+f) \left( \prod_i^{in} f_i \right) \left( \prod_j^{out} (1 \pm f_j) \right) - f \left( \prod_i^{out} f_i \right) \left( \prod_j^{in} (1 \pm f_j) \right) \tag{D.7}$$

$$= (1+f) (f_1 f_2) ((1-f_3)(1 \pm f_4)) - f (f_3 f_4) ((1-f_1)(1 \pm f_2)) \tag{D.8}$$

$$= (f_1 f_2) (1-f_3) + f f_1 f_2 (1-f_3) - f f_3 f_4 (1-f_1) \tag{D.9}$$

$$= f_1 f_2 - f_1 f_2 f_3 + f f_1 f_2 - f f_1 f_2 f_3 - f f_3 f_4 + f f_1 f_3 f_4 \tag{D.10}$$

We can assume that the distribution function of the ions has not changed after

the process; hence,  $f_2 \approx f_4$ . This will cancel out the fourth and the last term,

$$\mathbb{F} = f_1 f_2 (1 - f_3 + f) + f f_2 f_3 \quad (\text{D.11})$$

When the basin starts to form, we can assume that  $f \ll 1$ . The last term is an  $\epsilon^2$  term as  $f, f_2 \ll 1$ . This leaves us with,

$$\mathbb{F} = f_1 f_2 (1 - f_3) \quad (\text{D.12})$$

We plug this distribution factor in our current form of  $Q_B$ ,

$$Q_B = \frac{4g_1 g_2 g_3 g_4}{32(2\pi)^{11}} \frac{Z_j^2 e^4 g_{aee}^2}{m_e^4} \int d^3 k \int d^3 p_1 \int d^3 p_2 \int d^3 p_3 \int d^3 q \\ \delta^3(\vec{p}_1 - \vec{p}_3 + \vec{q}) \delta \left( \frac{\vec{p}_1^2 - \vec{p}_3^2}{2m_e} - m \right) \frac{1}{\vec{q}^2 + \kappa_s^2} f_1 f_2 (1 - f_3) \quad (\text{D.13})$$

We can now integrate out  $\int d^3 p_3$  over the remaining  $\delta^3$  function. It will fix  $\vec{p}_3 = \vec{p}_1 - \vec{q}$ . Apart from that, we can integrate out  $\int d^3 p_2 \frac{g_2 f_2}{(2\pi)^3} = n_j$ , giving us,

$$Q_B = \frac{4g_1 g_3 g_4}{32(2\pi)^8} \frac{\bar{n}_N e^4 g_{aee}^2}{m_e^4} \int d^3 k \int d^3 p_1 \int d^3 q \\ \delta \left( \frac{\vec{p}_1^2 - \vec{p}_3^2}{2m_e} - m \right) \frac{1}{\vec{q}^2 + \kappa_s^2} f_1 (1 - f_3) \quad (\text{D.14})$$

where  $n_j Z_j^2 = \bar{n}_N$ .

# Appendix E

## Dark Currents for CCD

A good explanation of Dark Currents (DC) and their role in CCD detection is given in [61]. A summary of DC is provided in this appendix for quick reference.

To understand the origin of DC, it is essential to recall how a Charge-Coupled Device (CCD) works. CCDs are built by using semiconductors like Silicon. A comparison of metals, insulators, and semiconductors is shown in fig.(E.1).

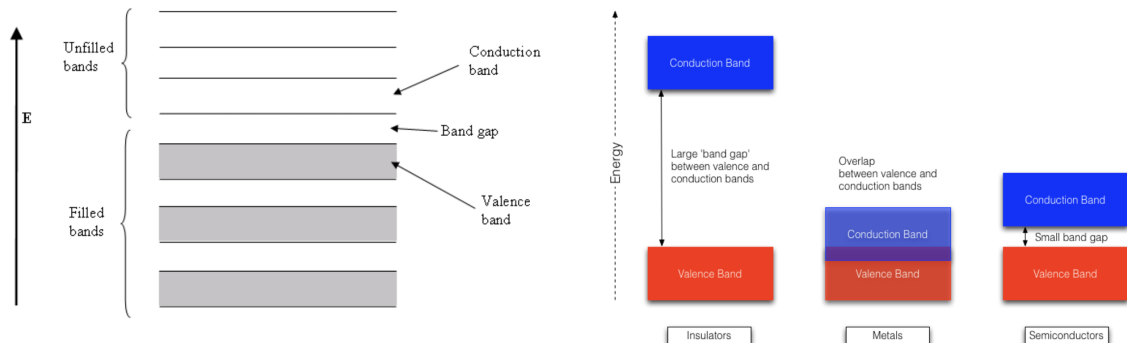


Figure E.1: *Left:* Band structure of electron energy in a solid. *Right:* The difference between the band gaps in insulators, metals, and semiconductors. The figure is taken from [61].

As shown in the figure above, semiconductors have small band gaps. Electrons can be promoted into the conduction band by absorbing energy as a photon. This property of semiconductors allows them to be used in CCDs as photon detectors.

Photons excite electrons into the conduction band. These electrons are free to move through the CCD and so can be moved to some readout electronics, which counts the number of electrons that have been excited. The number of electrons counted is proportional to the number of photons arriving at the detector. CCDs thus have to perform four jobs:

1. Create photo-electrons
2. Store photo-electrons in pixels during exposure to photons
3. Move the photo-electrons to the readout electronics
4. Count the number of photo-electrons created in each pixel

**Dark Currents** The photo-electrons are produced in CCDs when photons excite electrons from the valence to the conduction band. Photo-electrons can also be generated by thermal excitation, i.e., thermal excitation can produce electrons in the conduction band. These thermally excited electrons are indistinguishable from photo-electrons. The electrons in the conduction band due to thermal excitations contribute to our measurement. These contributions are known as Dark Currents. Devices are calibrated to account for their dark currents by taking Dark Frames. Dark Frames correspond to the data taken with a closed shutter on a CCD. Dark Frame data is considered when analyzing the actual data collected by the CCD.

# **Statement of Authorship**

I herewith declare that this thesis was solely composed by myself and that it constitutes my own work unless otherwise acknowledged in the text. I confirm that any quotes, arguments or concepts developed by another author and all sources of information are referenced throughout the thesis. This work has not been accepted in any previous application for a degree.

Montreal, September 30, 2022



---

Signature